https://doi.org/10.5194/egusphere-2026-3382
Preprint. Discussion started: 7 July 2026

Evaluation of the GOSAT/GOSAT-2 XCO_2 proxy XCH_4 product by comparison with TCCON observations over China

Xinran Jiang[1,2], Gerrit de Leeuw[1,3], Cheng Fan[1,*], Jeon-Teo Dong[4], Zhengqiang Li[1,2]

[1]State Key Laboratory of Remote Sensing and Digital Earth, Aerospace Information Research Institute, Chinese Academy of Sciences, Beijing 100101, China
[2]University of Chinese Academy of Sciences, Beijing 100049, China
[3]Royal Netherlands Meteorological Institute (KNMI), R&D Satellite Observations, P.O. Box 201, 3730AE De Bilt, The Netherlands
[4]Satellite Application Center for Ecology and Environment, Ministry of Ecology and Environment of People's Republic of China, Beijing 100094, China

Correspondence: Dr. Cheng Fan (fancheng@aircas.ac.cn)

Abstract. Methane (CH_4) is the second most important greenhouse gas after carbon dioxide (CO_2) and its accurate monitoring supports China's "dual carbon" goals. Satellites enable global monitoring of CH_4, supported by various sensors and retrieval techniques. Among them, the XCO_2 proxy method derives the column-averaged dry-air mole fraction of CH_4 (XCH_4) from the XCH_4/XCO_2 ratio and an independent estimate of XCO_2. By exploiting the overlapping absorption bands of CH_4 and CO_2 near 1.6 μm and assuming similar vertical distributions, the ratio eliminates common retrieval errors, providing an accurate estimate of XCH_4. In this study, four XCO_2 proxy methane products, GOSAT SRPR, OCPR, FOCAL Proxy, and GOSAT-2 SRPR, are evaluated using TCCON ground-based observations at the Hefei and Xianghe sites in China. The comparison shows that the GOSAT products (OCPR, SRPR, FOCAL Proxy) are more accurate at Xianghe, while GOSAT-2 products (SRPR) are similar at both sites with better performance than each of the GOSAT products (>50% meeting GCOS requirements). All products, except OCPR, overestimate XCH_4 at Hefei and underestimate XCH_4 at Xianghe, which stems from both XCO_2 prior model errors and spatial inconsistency between satellite and ground-based measurements. Furthermore, the overestimation of the ratio implies that the fundamental assumption of the XCO_2 proxy method is not fulfilled, primarily due to bias in raw XCH_4. This study provides key error characteristics and spatial-seasonal biases in current satellite proxy methane products over China, providing a scientific basis for future retrieval optimization.

1 Introduction

Methane (CH_4), as the world's second-largest anthropogenic greenhouse gas after carbon dioxide (CO_2), exerts a profound impact on the Earth' climate (Hansen and Sato, 2001). Since the end of the 20th Century, the rapid increase of globally averaged CH_4 concentrations has attracted widespread international concern, prompting numerous countries, including China, to establish "carbon neutrality" and "carbon peak" targets (Van Soest et al., 2021). Following the Sixth Assessment Report (AR6), released by the Intergovernmental Panel on Climate Change (IPCC) in 2023, global surface temperatures are undergoing significant shifts. The global surface temperature for the period 2011–2020 increased by 1.09°C relative to 1850–1900, with human activities contributing an estimated 1.07°C. Well-mixed greenhouse gases (GHGs) contributed an estimated 1.0°C–2.0°C to warming, which was partially offset by anthropogenic aerosol cooling (IPCC, 2023). Recent data from the World Meteorological Organization (WMO) (WMO, 2025) indicates that the 2024 global mean near-surface temperature reached 1.55 ± 0.13 °C above pre-industrial levels, marking the first calendar year in the 175-year observational record with an annual mean temperature exceeding 1.5 °C. It should be noted that this single-year value is significantly influenced by natural variability such as El Niño events, and does not indicate that the long-term warming trend of the climate system has systematically crossed the 1.5 °C threshold set by the Paris Agreement. The latest 2025 climate report (WMO, 2026) records a slight temper-

https://doi.org/10.5194/egusphere-2026-3382
Preprint. Discussion started: 7 July 2026

ature drop to 1.43 °C, while the overall warming trend and climate imbalance continue to worsen. As CH_4 has a much shorter atmospheric lifetime than CO_2, its rapid reduction is more achievable and could mitigate ~0.3°C of warming on short term at no additional cost (UNEP, 2021). Although the atmospheric concentration of CH_4 is less than 1% of that of CO_2, the 20-year Global Warming Potential (GWP20) for fossil and non-fossil CH_4 is 82.5 and 79.7 times that of CO_2, while the 100-year GWP (GWP100) stands at 29.8 and 27.0 (IPCC, 2021). The Global Methane Pledge (GMP) proposes a 30% reduction in methane emissions by 2030 to mitigate the rate of global warming (Predybaylo et al., 2025). China, currently the world's largest methane emitter, plays a decisive role in these efforts (Alvarez et al., 2018; Tian et al., 2022). To support such climate actions, the Global Climate Observing System (GCOS) has set stringent requirements for column-averaged dry-air methane (XCH_4) observations, specifying a breakthrough measurement uncertainty (2-sigma) of 10 ppb and a long-term stability of 2 ppb/decade (GCOS, 2022).

As a potent greenhouse gas, the accurate quantification of methane emissions is important for climate mitigation and a critical factor for nations to fulfill international emission reduction responsibilities (Costantiello et al., 2025). Satellite remote sensing, characterized by its extensive spatial coverage and consistent global measurement standards, has become a core instrument for monitoring methane concentrations (Jacob et al., 2016). However, satellite observations are limited to spectral radiance intensities. Retrieving XCH_4 mole fractions (i.e. the vertical column density of CH_4 divided by the vertical column density of dry air) requires high-precision algorithms to solve the radiative transfer equation, which accounts for atmospheric and surface optical properties (Bovensmann et al., 1999). While satellite data provide the basis for concentration monitoring, determining emissions further necessitates inversion models that accurately describe atmospheric physical transport processes. Consequently, the development of efficient and robust retrieval algorithms poses a central challenge in satellite methane remote sensing research.

Satellite retrieval methods for methane are primarily categorized into two categories: physics-driven methods and data-driven methods. Physics-driven methods are based on radiative transfer theory, extracting concentration information by simulating the absorption and scattering of solar radiation within the atmosphere. A Full Physics (FP) algorithm (Hu et al., 2016; Lorente et al., 2022) constructs rigorous radiative transfer equations and employs iterative optimization techniques to simultaneously retrieve methane concentrations and auxiliary parameters, such as aerosol properties and surface albedo, thereby achieving an optimal estimation of the atmospheric state. To enhance computational efficiency, certain physical methods adopt specific simplification strategies. Differential Optical Absorption Spectroscopy (DOAS) (Buchwitz et al., 2000; Schneising et al., 2008; Schneising et al., 2019) focuses on the Beer-Lambert Law to extract narrow-band gas absorption signals through spectral filtering, while the Photon Path Length Probability Density Function (PPDF) (Oshchepkov et al., 2008; Andrey et al., 2013) utilizes probability distribution functions from a statistical physics perspective to describe the equivalent path length of photons, correcting for optical path offsets induced by multiple scattering. Data-driven methods—such as machine learning and deep learning algorithms—bypass explicit physical formulations, but utilize large-scale datasets to identify complex nonlinear mappings between observed spectra and methane concentrations, offering a highly efficient alternative for large-scale data processing.

The Proxy method (Parker et al., 2015; Parker et al., 2020) serves as a simplified retrieval scheme within the physics-driven framework. The Proxy method requires the use of a sensor which measures high-resolution spectra over a wavelength range that is sensitive to both gases (in this case CH_4 and CO_2) in close proximity. Taking advantage of the overlapping absorption bands of CH_4 and CO_2 near 1.6 μm and assuming similar vertical distributions, the spectral radiances observed by the sensor in this waveband have traversed similar optical paths, which thus ensures similar atmospheric perturbations and surface effects. By retrieving the vertical column densities or column-averaged dry air mole fractions (XCH_4 and XCO_2) and calculating the ratio (XCH_4/XCO_2), systematic optical path errors induced by aerosol scattering, surface reflection, and other atmospheric effects are effectively eliminated. The XCO_2 Proxy method discussed in this study, refers to the retrieval of XCH_4, by multiplication of the ratio with an independent estimate of XCO_2, such as XCO_2 model data. As compared to XCH_4, XCO_2 is relatively stable and therefore serves as a reliable reference for accurate XCH_4 retrieval. Due to its robust physical performance when addressing complex atmospheric interference, the Proxy algorithm has been extensively implemented across multiple major satellite missions (Schepers et al., 2012). Compared with conventional full-physics retrievals, this method exhibits lower sensitivity to instrument-level inconsistencies (e.g., radiometric calibration drift and spectral band mismatching), and is more robust against instrument-related biases, making it more suitable for long-term dataset retrievals. In addition, its inherent tolerance to moderate aerosol scattering significantly improves the effective data yield, especially in complex atmospheric environments (Chevallier et al., 2010; Parker et al., 2015).

In this study, the quality of different products resulting from application of the XCO_2 Proxy method to retrieve XCH_4 from GOSAT and GOSAT-2 observations over China will be evaluated through comparison with ground-based data from the Total Carbon Column Observing Network (TCCON) sites at Hefei and Xianghe. The results of this comparison are expected to provide a scientific basis for the monitoring and assessment of methane emissions in China, thereby contributing data and analysis results from satellite observations over China to global methane emission research.

2 Data

2.1 GOSAT/GOSAT-2

In this study, data products are used from the Greenhouse Gases Observing Satellite (GOSAT) and its successor, GOSAT-2. GOSAT was launched on January 23, 2009, through a joint effort by the Japan Aerospace Exploration Agency (JAXA), the Japanese Ministry of the Environment (MOE), and the National Institute for Environmental Studies (NIES). GOSAT was the world's first scientific satellite dedicated to the precise monitoring of CO_2 and CH_4 concentrations from space (Yokota et al., 2009). Its core scientific mission aims to fill greenhouse gas monitoring gaps over oceans and remote regions via high-frequency global observations, to accurately assess carbon sources and sinks at sub-continental scales, and to improve the understanding of global carbon cycle mechanisms and their impacts on climate change (Butz et al., 2011). GOSAT operates in a sun-synchronous quasi-recurrent orbit at an altitude of approximately 666 km and an inclination of about 98°, with a local equator crossing time at 13:00±15 minutes and a revisit period of 3 days, ensuring high-frequency coverage for most parts of the Earth.

The primary payload aboard GOSAT is the Thermal and Near-infrared Sensor for Carbon Observation (TANSO), which consists of two components: the Fourier Transform Spectrometer (TANSO-FTS) and the Cloud and Aerosol Imager (TANSO-CAI) (Yokota et al., 2009). TANSO-FTS measures radiation in four spectral bands including the near infrared band at 0.76 μm (oxygen absorption band), two Short-Wave Infrared (SWIR) bands at 1.6 μm (CO_2 and CH_4 absorption bands) and 2.0 μm (CO_2), and a wide Thermal Infrared (TIR) band extending from 5.5 to 14.3 μm. The spectral resolution of the SWIR bands (Bands 1-3) is approximately 0.27 cm^{-1} (full width at half maximum, FWHM). Spectra of reflected solar radiation and thermal radiation emitted by the Earth-atmosphere system are analyzed and the intensities of characteristic absorption lines are used to retrieve the total columns and vertical distributions of the concentrations of CO_2 and CH_4. The nadir footprint diameter of TANSO-FTS is approximately 10.5 km (Kuze et al., 2016). TANSO-CAI utilizes four channels with wavelengths ranging from the visible to the near-infrared to simultaneously acquire cloud and aerosol information along the observation path at spatial resolutions of 0.5 km to 1.5 km. This information is used to filter out contaminated data and perform atmospheric corrections (Yokota et al., 2009). Over land, the instruments primarily use a nadir observation mode, whereas, over ocean they observe in the sun glint to capture solar specular reflection to improve the signal-to-noise ratio. GOSAT's design objective is to control the relative observation precision of CO_2 and CH_4 within 4 ppm (approximately 1%) and 34 ppb, respectively, providing robust scientific data supporting the implementation of global climate agreements and the formulation of carbon emission reduction policies (Butz et al., 2011).

https://doi.org/10.5194/egusphere-2026-3382
Preprint. Discussion started: 7 July 2026

GOSAT-2 was launched on October 29, 2018, and operates in a sun-synchronous quasi-recurrent orbit at an altitude of approximately 613 km with a local equator crossing time at 13:00 and a revisit period of 6 days. GOSAT-2 aims to further quantify the global carbon budget through observations with higher-precision than GOSAT (Kuze et al., 2009). Its core payload is TANSO-FTS-2, with an expanded spectral coverage of five bands, adding the capability to detect carbon monoxide (CO). The spectral resolution in the SWIR of approximately 0.2 cm⁻¹ is better than that of TANSO-FTS, enabling finer discrimination of absorption lines. The mission achieves significantly improved concentration measurement precision, with target uncertainties of 0.5 ppm for CO_2 and 5 ppb for CH_4 over a 500 km spatial mesh and with a 1-month observational period (Imasu et al., 2023; Eoportal, 2024). In terms of observation methodology, GOSAT-2 introduced "intelligent pointing" technology, which utilizes a forward-looking camera to identify and avoid clouds in real-time. This significantly improves the acquisition efficiency of valid clear-sky observation data, with its detection footprint optimized to 9.7 km (Kuze et al., 2009). Furthermore, GOSAT-2 features enhanced sensor agility, characterized by a broader and more flexible pointing range compared to its predecessor. This increased manoeuvrability allows the satellite to better adapt to complex terrain and rapidly adjust its optical axis to capture clear-sky scenes in fragmented cloud conditions (Imasu et al., 2023). GOSAT-2 inherits and extends the observational capabilities of GOSAT, and the data from both satellites complement each other, providing a continuous observational record for studying long-term changes in greenhouse gases (Buchwitz et al., 2017).

2.2 TCCON data

TCCON (Wunch et al., 2015; Laughner et al., 2024) is a global network of ground-based Fourier Transform Spectrometers (FTS) that measure direct near-infrared solar spectra within the 4000–9000 cm⁻¹ range, with temporal high-resolution. At these wavelengths, adverse effects of high uncertainties associated with scattered light are avoided. These spectra are used to retrieve vertical column densities of a variety of gases, such as CO_2, CH_4, N_2O, HF, CO, H_2O, and HDO, using a non-linear least-squares spectral fitting algorithm. Ground-based FTS observations achieve exceptionally high precision; the single measurement precision for XCO_2 is approximately 0.15% (~1 ppm) and for XCH_4 it is 0.2% (Toon et al., 2009). To ensure global consistency across stations, TCCON data are calibrated using airborne in situ measurements, yielding an estimated accuracy of 0.8 ppm for carbon dioxide and 7 ppb for methane. These high-precision observational data serve as a reference for the validation of satellite-retrieved greenhouse gas products such as CO_2 and CH_4 (Wunch et al., 2010).
Established in 2004, TCCON joined the WMO Global Atmosphere Watch (GAW) as a contributing network in 2009. Currently, China hosts two TCCON stations: the Hefei station and the Xianghe station (Hong et al., 2024).

2.2.1 Hefei

The Hefei station is located within the campus of the Anhui Institute of Optics and Fine Mechanics, Chinese Academy of Sciences (AIOFM-CAS), in the western suburbs of Hefei, Anhui Province, China. The site is adjacent to the 207.5 km² Shushan Lake (the Dongpu Reservoir) to the southwest (see Fig. 1a) (Wang et al., 2017). The immediately adjacent, extensive water surface acts as a natural buffer, effectively mitigating direct interference from localized urban emissions. The region is characterized by prevailing southeasterly winds in summer and northwesterly winds in winter. Relevant information is provided in Table 1.
Hefei was the first observation station in China that joined TCCON. The instrumentation includes a high-resolution FTS (IFS125HR, Bruker, Germany), a solar tracker (Tracker-A Solar 547, Bruker, Germany), and a meteorological station (ZENO 3200, Coastal Environmental Systems, USA). Since its installation in April 2014, the instrument has operated almost continuously, with the exception of a two-months data gap between December 2014 and February 2015 due to scanner issues. Prior to July 27, 2015, only near-infrared (NIR) solar spectra were collected; since then, NIR and mid-infrared (MIR) solar spectra have been collected alternately during routine observations (Wang et al., 2017). The core measurement objectives of this station include the total column concentrations and vertical mixing ratio profiles of CO_2, CH_4, and other key greenhouse gases

(Zhou et al., 2022). The Hefei site is also part of the Sun-Sky Radiometer Observation Network (SONET), employing a sun photometer to track aerosol optical characteristics synchronously (Li et al., 2018).

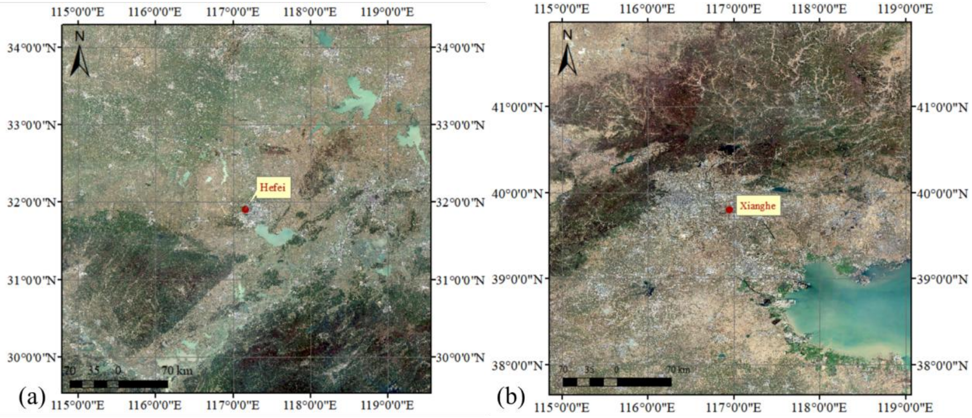

Figure 1. Locations of the TCCON stations used in this study: (a) Hefei site and (b) Xianghe site. Sources: Copernicus Sentinel-2 | Powered by Esri.

2.2.2 Xianghe

The Xianghe station is located in Daluotun Village, Shuyang Town, Xianghe County, Hebei Province, China. Relevant information is provided in Table 1. The station is run by the Institute of Atmospheric Physics, Chinese Academy of Sciences. Situated approximately 50 km east of Beijing and 70 km north of Tianjin, the station is located at a transportation and transit hub within the Beijing-Tianjin-Hebei region (see Fig. 1b) (Ran et al., 2016). Xianghe County experiences a mid-latitude monsoon climate, characterized by prevailing southeasterly winds in summer and northwesterly winds in winter. The maximum summer temperature can reach 38°C, while the minimum winter temperature drops to −10°C. Precipitation mainly occurs in the summer, with occasional extreme precipitation events when daily rainfall exceeds 100 mm. The surface type surrounding the station consists of desert and rock, with flat terrain typical of rural areas. There are small towns, farmland, and irrigated agricultural zones in the vicinity of the Xianghe station. The region is influenced by emissions from significant greenhouse gas sources, particularly of anthropogenic origin, and is further influenced by emissions from major cities such as Beijing and Tianjin, resulting in a certain degree of air pollution. Heavy pollution occurs under weather conditions conducive to the formation of haze. The geographical location of the Xianghe station makes it a critical site for studying greenhouse gas emissions and atmospheric pollution in North China. Operating since 1974, the station was upgraded in June 2018 with a high-resolution FTS (Bruker IFS 125HR, Germany) and a solar tracker (A547, Bruker, Germany) for solar absorption measurements. This system primarily measures XCO_2, XCH_4 and XCO (Ji et al., 2020; Zhou et al., 2022). Additionally, a CIMEL CE318 sun photometer (Cimel Electronique, France) has been operational at the site as part of the Aerosol Robotic Network (AERONET), providing synchronous measurements of aerosol optical properties (Li et al., 2007).

Table 1 TCCON site information

Site	Geographical Location, elevation	Data availability	Surface Albedo	Reference
Hefei	31.9N, 117.17 E, 30 m	2015.11.02-2024.12.29	0.15–0.35	Wang et al. (2017)
Xianghe	39.8 N,116.96 E, 36 m	2018.06.14-2023.05.29	0.15–0.45	Yang et al. (2020)

2.3 CO_2 Proxy retrieval algorithms and data products

Based on the principles detailed in the Introduction, the XCO_2 Proxy algorithm retrieves XCH_4 by calculating the ratio of the columns retrieved in the 1.65 µm (CH_4) and 1.61 µm (CO_2) absorption bands to cancel out common optical path errors. The final XCH_4 is derived as follows:

$$\mathrm{XCH_4(Proxy)}=\frac{\mathrm{XCH_4}}{\mathrm{XCO_2}} \times \mathrm{XCO_2(model)} \quad (1)$$

where XCO_2 (model) represents the independent XCO_2 estimate derived from atmospheric transport models. This model-based value serves as a reliable reference to scale the retrieved ratio into absolute XCH_4, while ensuring robustness against scattering interference.

In this study, four proxy XCH_4 products derived from three distinct algorithms were selected: OCPR, SRPR, and FOCAL Proxy, with SRPR products from application to both GOSAT and GOSAT-2. The basic specifications of these products are summarized in Table 2. Detailed descriptions of the principles underlying each algorithm are provided in the following sub-sections.

Table 2 Proxy XCH_4 Products used in this study

Satellite	Spatial resolution	Product	Version	Time span	Bias correction
GOSAT	Φ10.5 km	SRPR XCH_4	v2.3.9	2016.01–2023.12	Wu (2021a)
		OCPR XCH_4	v9.0	2016.01–2022.12	Boesch and Di Noia (2023)
		FOCAL Proxy XCH_4	v3.0	2021.11–2023.12	Noël et al. (2022)
GOSAT-2	Φ9.7 km	SRPR XCH_4	v2.0.1	2019.02–2023.12	Barr and Borsdorff (2023)

2.3.1 OCPR XCH_4 algorithm

The OCPR (OCO-2 Proxy) algorithm was developed by the University of Leicester and is currently maintained by the Institute of Environmental Physics (IUP) at the University of Bremen. As a core component of the Copernicus Climate Change Service (C3S) greenhouse gas suite, this algorithm processes SWIR spectral data from the GOSAT satellite (Boesch et al., 2024; Boesch and Di Noia, 2023). Technically, OCPR employs a decoupled retrieval strategy—distinct from coupled schemes—by independently retrieving XCH_4 and XCO_2 from the 1.65 µm (CH_4) and 1.61 µm (CO_2) bands before calculating their ratio to mitigate light-path errors. The independent estimate of XCO_2 used in the OCPR algorithm is the median of multi-model ensemble XCO_2 prior data from GEOS-Chem (Bey et al., 2001; Peters et al., 2007), NOAA Carbon Tracker (Peters et al., 2007), and LMDZ/MACC-II (Hourdin et al., 2006; Inness et al., 2013). Comparison of the v9.0 product used in this study with TCCON shows a bias, and a fixed global correction factor of -9.06 ppb has been officially adopted to compensate for the observed mean bias (Parker et al., 2020).

The OCPR data product was validated against ground-based TCCON observations, as detailed in the Product User Guide and Specification (PUGS) (Boesch and Di Noia, 2023). For land observations between April 2009 and December 2017, the mean bias and standard deviation of the XCH_4 OCPR product are -1.25 ppb and 13.81 ppb. (Boesch and Di Noia, 2023).

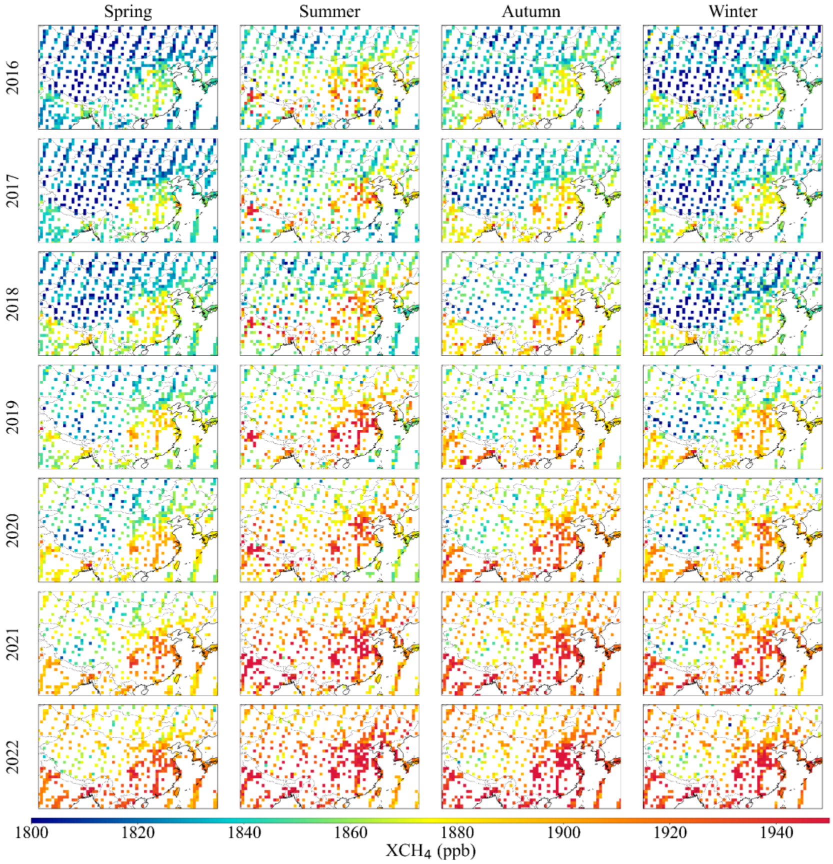

Figure 2. Maps of seasonal mean of GOSAT OCPR XCH_4 for the years 2016-2022.

The spatial distributions of XCH_4 across the study area, retrieved from GOSAT using the OCPR algorithm, are presented in Fig. 2 as seasonal averages in each of the years 2016 to 2022. The maps in Fig. 1 show the significant year-to-year increase of XCH_4, with strong seasonal differences, and spatial variations across China with a pronounced "high in the southeast and low in the northwest" pattern. High XCH_4 occurs primarily over densely populated and highly industrialized regions in Southeast China. The seasonal variations, with highest concentrations during the summer and lowest during the spring, are closely related to methane emissions (East et al., 2024). The spatiotemporal variations stem not only from anthropogenic emissions, such as industrial and agricultural activities, but is also significantly modulated by the seasonal enhancement of biogeochemical processes, wetland emissions (East et al., 2024) and rice cultivation (Shen et al., 2024).

2.3.2 SRPR XCH_4 algorithm

The SRPR (SRON-RemoTeC Proxy) algorithm was developed by the Space Research Organization Netherlands (SRON) (Wu, 2021b; Butz et al., 2009; Butz et al., 2010). SRPR employs a coupled retrieval scheme that simultaneously fits CH_4 and CO_2 within a single state vector to ensure consistent light-path treatment. To derive the final XCH_4 product, XCO_2 from the CAMS model (Lloret et al., 2024; Agustí-Panareda et al., 2023) is incorporated as the independent estimate.

To ensure the required high precision, the SRPR XCH_4 products undergo a systematic bias correction to mitigate retrieval errors stemming from the algorithm's sensitivity to surface albedo, particularly in the 1.6 µm band. According to the PUGS (Barr and Borsdorff, 2023; Wu, 2021a), comparison of satellite retrievals with TCCON measurements reveals a significant correlation between retrieval bias and the surface albedo in the 1.6 µm band. Consequently, a linear bias correction model was established for land observations:

$$\mathrm{XCH_{4corr}} = \mathrm{XCH_4} \times (\mathrm{a} + \mathrm{b} \times \alpha) \tag{2}$$

where α represents the surface albedo. $\mathrm{XCH_{4corr}}$ is the corrected result, while XCH_4 is the original result before correction. In this study, the GOSAT (Version 2.3.9) and GOSAT-2 (Version 2.0.1) products are utilized, which officially incorporate this bias correction scheme based on the coefficients specified in the PUGS documentation. For GOSAT, correction coefficients are tuned by gain mode: high-gain mode (low albedo): a = 0.9869, b = 0.01788; medium-gain mode (high albedo): a = 0.98446, b = 0.01892 (Wu, 2021a). For the GOSAT-2 land observations, these coefficients were refined to a=0.99274, b=0.00158 (Barr and Borsdorff, 2023). All correction parameters were obtained from regression of the GOSAT observations on the TCCON reference values. The minimal b value results in nearly constant bias correction across varying levels of surface albedo (α), indicating a remarkably low sensitivity to surface brightness. In a recent publication by Barr et al. (2025), only the parameter a was used for the proxy bias correction. These authors also applied quality filtering based on a random forest model, which further improved the product.

The precision of the GOSAT SRPR product exhibits significant mode dependency. The high-gain mode shows the best quality, validated against 12 global TCCON stations (not including Chinese sites) from 2009 to mid-2020: mean bias of 0.68 ppb, single-point standard deviation of 14.49 ppb, and correlation coefficient of 0.91(Wu, 2021b). The GOSAT-2 SRPR XCH_4 validation covers 2019 – 2022 using 21 TCCON stations, including Hefei and Xianghe in China. It achieves a post-correction global mean bias of -0.14 ppb, a single-point standard deviation of 18.09 ppb, and a correlation coefficient of 0.80 (Barr et al., 2023; Barr and Borsdorff, 2023).

The spatial distributions of GOSAT and GOSAT-2 SRPR derived XCH_4 are presented in the maps in Figs. A1 and A2 (see Appendix A), showing seasonal averages for the years 2016 – 2023 (GOSAT) and 2019 – 2023 (GOSAT-2).

2.3.3 FOCAL Proxy XCH_4 algorithm

The Fast atmospheric traCe gAs retrievaL (FOCAL) algorithm has been developed by the IUP, University of Bremen (Noël et al., 2021). Within its forward model, FOCAL incorporates a single scattering layer approximation to simulate the atmospheric light path. This mechanism explicitly accounts for the scattering effects of aerosols and thin clouds during the simultaneous retrieval of XCH_4 and XCO_2 total columns (Noël et al., 2022). To derive the final proxy XCH_4 data, the ratio of these retrieved columns is multiplied with independent XCO_2 estimates from the SLIMCO2 model (Reuter et al., 2020) following the normalization procedure outlined in Sect. 2.2.

To account for the non-linear residual biases and the underestimation of error bars inherent in the proxy method, the IUP Bremen team has implemented a two-step post-processing calibration for the FOCAL Proxy XCH_4 product (Version 3.0), consisting of bias correction and uncertainty recalibration (Noël et al., 2022). The bias correction utilizes a Random Forest Regression model with 10 predictors such as retrieved water vapor, solar zenith angle, and solar-induced chlorophyll fluorescence to refine the retrieved XCH_4. Subsequently, the uncertainty recalibration is performed via a linear function to ensure that the final uncertainty parameters accurately reflect the dispersion of the retrieved values relative to the reference benchmark:

$$\Delta\mathrm{X} = \mathrm{a_c} + \mathrm{b_c}\Delta\mathrm{X_{retr}} \tag{3}$$

where ΔX_{retr} represents the raw uncertainty generated by the proxy method. The coefficients are set to a_c=7.951 ppb and b_c =0.67 to ensure that the corrected uncertainty realistically reflects the dispersion of the retrieved values relative to the reference data (Noël et al., 2021; Noël et al., 2022). Validation against TCCON data demonstrates that the FOCAL Proxy XCH_4 product exhibits exceptional retrieval accuracy. For the GOSAT satellite, the mean bias of single observations is approximately -2.10 ppb with a standard deviation of 13.59 ppb. The seasonally averaged spatial distributions of the GOSAT FOCAL Proxy XCH_4 product over China for the years 2021-2023 are presented in Fig. A3 of Appendix A.

2.4 Aerosol Optical Depth (AOD) Supplementary Data

To evaluate the influence of aerosol loading on the retrieval accuracy of greenhouse gases, AOD data were incorporated in this study as a key auxiliary parameter. The AOD data were obtained from Sun photometers from the SONET site (Li et al., 2018) in Hefei and the AERONET site (Holben et al., 2001; Holben et al., 1998) in Xianghe. Sun photometers provide AOD from direct sun measurements, at a range of wavelengths, every 15 minutes during daylight hours. Figure 3 presents the daily mean time series of ground-based AOD at 1640 nm for the Hefei (orange) and Xianghe (blue) sites. The Hefei data set suffers from an approximately four-year data gap between 2018 and 2022, while data at the Xianghe station are available for the periods from March 2019 to June 2020 and from July 2022 to December 2023. The Xianghe site is a typical urban/industrial background station, whereas, the Hefei site represents a low-aerosol background. However, the frequency of high-AOD observations at the Xianghe site in Figure 3 is paradoxically lower than that at the Hefei site. This discrepancy is primarily attributed to sampling bias (Li et al., 2007): low visibility during extreme haze episodes at Xianghe often leads to tracking failures of the sun photometer, causing the most polluted data to be excluded from the valid statistics. Furthermore, the higher relative humidity in Hefei promotes hygroscopic growth (Li et al., 2014), which results in higher AOD, while the drier climate in Xianghe results in lower AOD for similar particle concentrations.

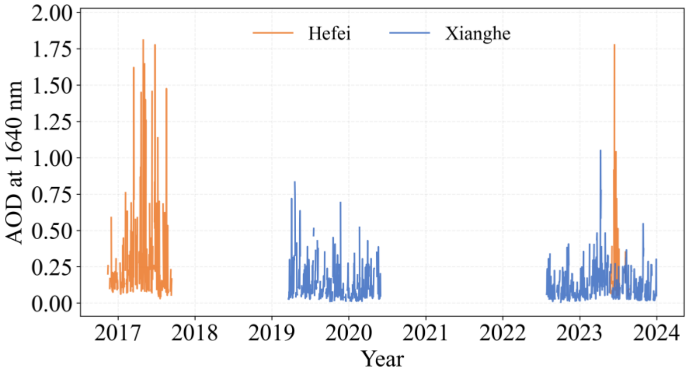

Figure 3. Daily mean time series of ground-based AOD at 1640 nm for the Hefei (orange) and Xianghe (blue) sites.

2.5 Validation Methods and Metrics

To quantitatively evaluate the accuracy and reliability of different retrieval algorithms, five key statistical metrics are introduced in this study: mean bias (Bias), root-mean-square error (RMSE), Pearson's correlation coefficient (R), centered root-mean-square error (CRMSE), and Normalized Standard Deviation (NSD). RMSE is used to quantify the overall difference between satellite retrievals and ground-based observations, accounting for both systematic bias and random fluctuations. CRMSE filters out the influence of the mean bias to specifically measure the variability of retrieval values relative to their own mean. These metrics are calculated as follows:

$$\mathrm{Bias} = \frac{1}{\mathrm{N}}\sum_{\mathrm{i}=1}^{\mathrm{N}}\left(\mathrm{X}_{\mathrm{proxy,i}} - \mathrm{X}_{\mathrm{TCCON,i}}\right) \tag{4}$$

$$\mathrm{RMSE} = \sqrt{\frac{1}{\mathrm{N}}\sum_{\mathrm{i}=1}^{\mathrm{N}}\left(\mathrm{X}_{\mathrm{proxy,i}} - \mathrm{X}_{\mathrm{TCCON,i}}\right)^2} \tag{5}$$

$$\sigma_{\mathrm{proxy}} = \sqrt{\frac{1}{\mathrm{N}-1}\sum\nolimits_{\mathrm{i}=1}^{\mathrm{N}}\left(\mathrm{X}_{\mathrm{proxy,i}} - \overline{\mathrm{X}}_{\mathrm{proxy}}\right)^2} \tag{6}$$

$$\mathrm{R} = \frac{\sum_{\mathrm{i}=1}^{\mathrm{N}}\left(\mathrm{X}_{\mathrm{proxy,i}} - \overline{\mathrm{X}}_{\mathrm{proxy}}\right)\left(\mathrm{X}_{\mathrm{TCCON,i}} - \overline{\mathrm{X}}_{\mathrm{TCCON}}\right)}{\sqrt{\sum_{\mathrm{i}=1}^{\mathrm{N}}\left(\mathrm{X}_{\mathrm{proxy,i}} - \overline{\mathrm{X}}_{\mathrm{proxy}}\right)^2}\sqrt{\sum_{\mathrm{i}=1}^{\mathrm{N}}\left(\mathrm{X}_{\mathrm{TCCON,i}} - \overline{\mathrm{X}}_{\mathrm{TCCON}}\right)^2}} \tag{7}$$

$$\mathrm{CRMSE} = \sqrt{\frac{1}{N}\sum_{i=1}^{N}\left[\left(X_{\mathrm{proxy},i} - \overline{X}_{\mathrm{proxy}}\right) - \left(X_{\mathrm{TCCON},i} - \overline{X}_{\mathrm{TCCON}}\right)\right]^2} \tag{8}$$

$$\mathrm{NSD} = \frac{\sigma_{\mathrm{proxy}}}{\sigma_{\mathrm{TCCON}}} \tag{9}$$

where N represents the total number of matched data points, $X_{\mathrm{proxy},i}$ denotes the i-th XCH_4 retrieved by the satellite proxy algorithm, $X_{\mathrm{TCCON},i}$ is the corresponding TCCON reference data, $\overline{X}_{\mathrm{proxy}}$ and $\overline{X}_{\mathrm{TCCON}}$ represent their respective arithmetic means and σ_{proxy} and σ_{TCCON} denote the standard deviations of the retrieved XCH_4 and the TCCON reference data.

The validation results are evaluated against the standards defined by the GCOS (GCOS, 2022), which stipulates a target accuracy of 10 ppb for XCH_4 products to support climate change studies.

3 Validation against TCCON

In this study, the quality control protocols specified in the respective product user manuals are strictly followed for all satellite datasets to ensure data reliability. Only observations with a quality flag of zero (xch4_quality_flag = 0) are selected for analysis, representing the highest retrieval quality. This filtering process inherently incorporates a series of rigorous screening criteria, including constraints on the convergence metric, SNR thresholds, and the exclusion of samples with extreme aerosol loading or significant surface albedo fluctuations (Boesch and Di Noia, 2023; Wu, 2021a; Barr and Borsdorff, 2023).

The XCH_4 data products retrieved from GOSAT and GOSAT-2 data, using the four proxy CH_4 retrieval algorithms discussed in Sect. 2.2, have been validated versus the TCCON reference data at the Hefei and Xianghe stations. GOSAT and GOSAT-2 observations within ±2.5° of each TCCON station were collected and for each overpass a spatial mean was calculated for all valid pixels within the matching area (Parker et al., 2020). TCCON measurements were averaged within ±2 hours of the satellite overpass time to account for short-term atmospheric variability and ensure a robust temporal match.

Given that the Xianghe station is situated within the polluted Beijing-Tianjin-Hebei region, local emissions can lead to significant increases in near-surface concentrations. Such local emission plumes can be sensitively detected by ground-based instruments but, due to spatial averaging effects, satellite observations often fail to capture localized enhancements. This discrepancy in spatial representativeness can introduce validation errors; thus, it is essential to filter out data affected by local pollution. In the Xianghe region, anthropogenic incomplete combustion is the primary source of co-emitted CO and CH_4, while biogenic sources like agriculture or wetlands have less influence on short-term variability. As demonstrated in Yang et al. (2020), a strong positive correlation (R=0.82) exists between the daily anomalies of XCO (ΔXCO) and XCH_4 (ΔXCH_4). Following the methodology of Yang et al. (2020), ΔXCO was used as a reliable diagnostic tracer to screen the data for regional pollution events. First, the data were detrended for seasonal and long-term variations and ΔXCO anomalies were used to represent net deviations from the background. Based on the analysis of the ΔXCO variations, +36 ppb was selected as the threshold value above which pollution occurs and these events were excluded for further analysis.

The XCO_2 Proxy method consists of three parts as explained in Sect. 2.2 and shown in Eq. (1). The first step is the retrieval of XCH_4 and XCO_2 and determine the ratio of the results. The second step is to determine an independent estimate of XCO_2, and the final XCH_4 result is obtained by the multiplication of this ratio with the independent estimate of XCO_2. Below each of the products is evaluated by comparison with TCCON reference data. We first validate the final XCH_4 product retrieved using the XCO_2 Proxy method described by Eq. (1) in Sect. 3.1, followed by an assessment of the individual intermediate components in Sects. 3.2 and 3.3.

3.1 Validation of XCH_4

Time series of XCH_4 at the Hefei (a-d) and Xianghe (e-h) sites are presented in Fig. 4. The datasets include four satellite retrieval products—OCPR, SRPR, FOCAL Proxy (indicated as FOCAL), all applied to GOSAT, and SRPR (2SRPR) applied to GOSAT-2—together with ground-based TCCON observations. To capture the long-term evolution and inter-annual fluctuations of XCH_4, a non-linear composite regression model was fitted to the data points: 345

$$y(t) = a_0 + a_1 \cdot t + a_2 \cdot \sin(2\pi t + a_3), \quad (10)$$

where y(t) denotes the fitted XCH_4 concentration at time t, and t is the time in fractional years. a_{0-3} represent the free fit parameters, which are iteratively determined using the non-linear least squares regression method.

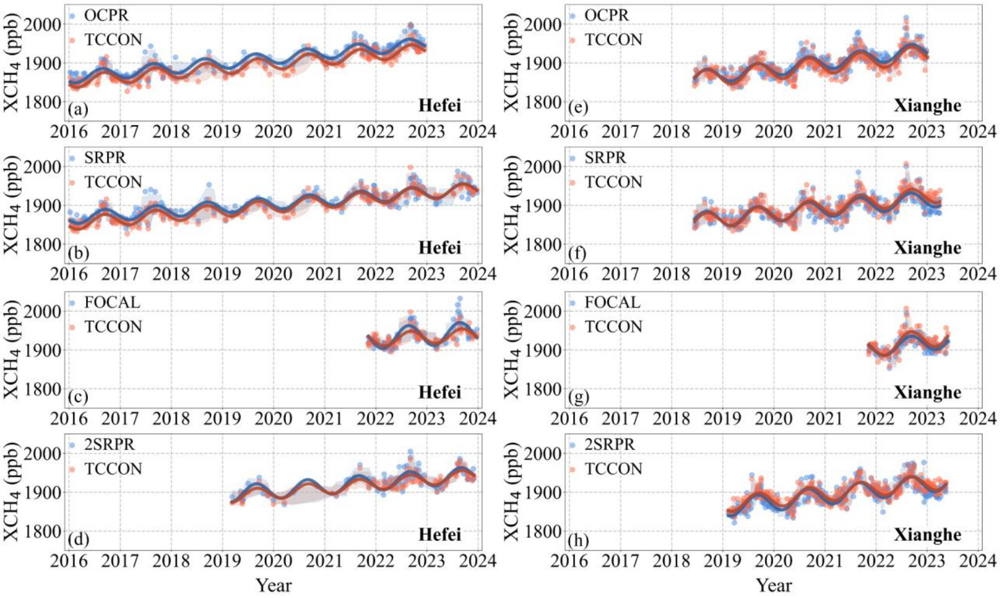

350 **Figure 4. Time Series of XCH_4 data retrieved by each algorithm (see legend and text), against TCCON reference data for the Hefei (a) (b) (c) (d) and Xianghe (e) (f) (g) (h) sites. The blue scatter points represent the XCO_2 Proxy XCH_4 products, the red scatter points denote the TCCON reference data, and the curves are the corresponding fitted lines calculated using Eq. (10). The shaded area represents the mean ± 1 standard deviation of the corresponding data points.**

https://doi.org/10.5194/egusphere-2026-3382
Preprint. Discussion started: 7 July 2026

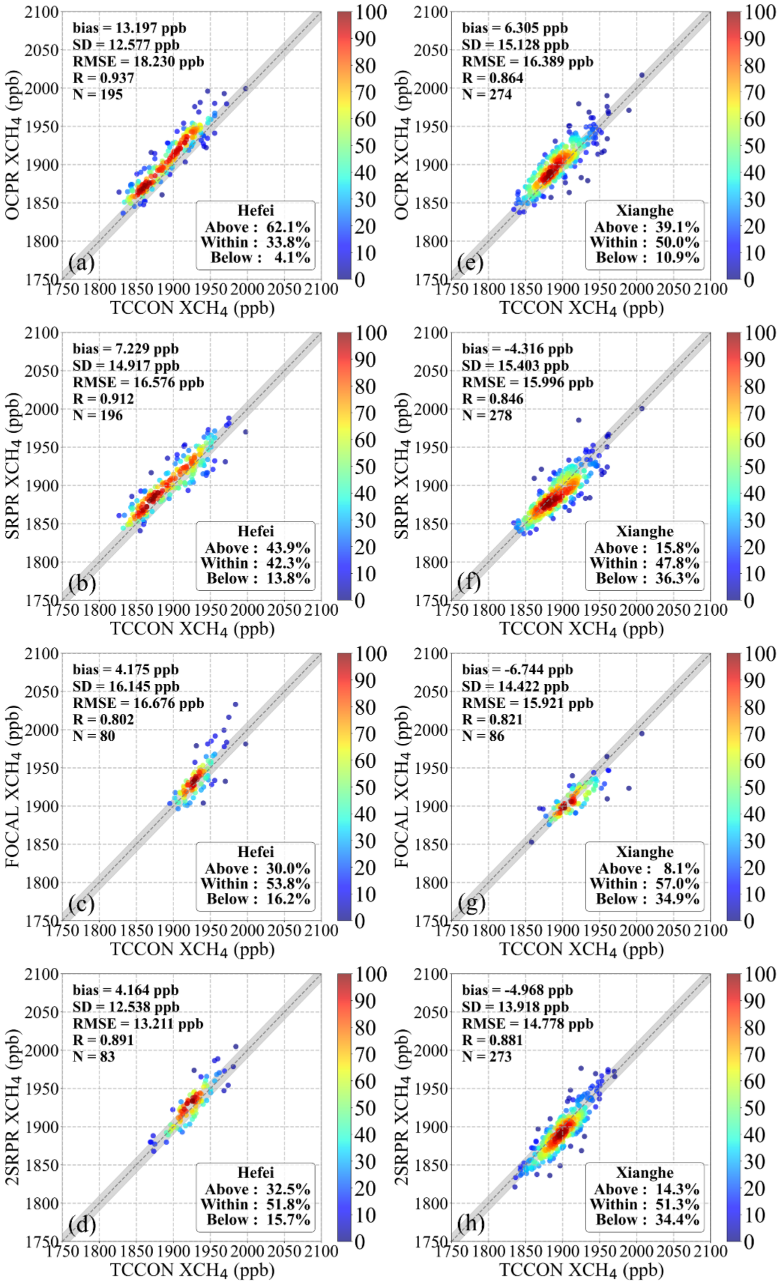

Figure 5. Scatter density plots of XCH4 data retrieved by each algorithm (as indicated along the vertical axes) against TCCON reference data for the individual Hefei (a) (b) (c) (d) and Xianghe (e) (f) (g) (h) sites. The density of the data points in % are color coded following the color bars to the right. Validation metrics are presented in the legend at the top-left. The dashed line indicates the 1:1 reference, with the grey shaded area representing an envelope of 10 ppb, consistent with the GCOS precision requirements for XCH4. "Within" denotes the percentage of data points within the GCOS envelope, while "Above" and "Below" represent the proportions of points falling above and below this range, respectively.

https://doi.org/10.5194/egusphere-2026-3382
Preprint. Discussion started: 7 July 2026

Table 3. Main statistics of the four Proxy XCH_4 products versus TCCON ground-based observations for the Hefei and Xianghe sites

Metric \ Product		GOSAT OCPR		GOSAT SRPR		GOSAT FOCAL Proxy		GOSAT-2 SRPR	
		Hefei	Xianghe	Hefei	Xianghe	Hefei	Xianghe	Hefei	Xianghe
Bias (ppb)		13.197	6.305	7.229	-4.316	4.715	-6.774	4.164	-4.968
RMSE (ppb)		18.230	16.389	16.576	15.996	16.676	15.921	13.211	14.778
R		0.937	0.864	0.912	0.846	0.802	0.821	0.891	0.881
SD (ppb)		12.577	15.128	14.917	15.403	16.145	14.422	12.538	13.918
N		195	274	196	278	80	86	83	273
GCOS: 10ppb	Above (%)	62.1	39.1	43.9	15.8	30.0	8.1	32.5	14.3
	Within (%)	33.8	50.0	42.3	47.8	53.8	57.0	51.8	51.3
	Below (%)	4.1	10.9	13.8	36.3	16.2	34.9	15.7	34.4

Figure 4 shows distinct seasonal cycles at both sites, with concentrations peaking in summer and autumn and minima in spring and winter. The number of ground-based observations at the Xianghe site is larger than at Hefei, which is attributed to its more advantageous meteorological conditions (Lorente et al., 2022). The methane concentrations at Hefei are larger than at Xianghe. The temporal variations of all four satellite products closely trace those of the TCCON observations, at both sites, but with some clear deviations too. At the Hefei site, the number of matched data samples was small between 2018 and 2021, which renders the evaluation of the data products more sensitive to outliers than in Xianghe, resulting in significant dispersion and larger uncertainty envelopes (shaded areas). To quantitatively evaluate these observations, site-specific scatter-density plots of the satellite products versus TCCON observations are provided in Fig. 5 and the statistical metrics are provided Table 3. The scatter-density plots show distinctly different bias at Hefei and Xianghe: all products show a systematic overestimation (positive bias) in Hefei, whereas at the Xianghe site, the bias for all products except OCPR is negative. In particular, the GOSAT OCPR XCH_4 is overestimated at the Hefei site (Fig. 4a), with a bias as high as +13.197 ppb and 62.1% of the data pairs above the GCOS requirement of ±10ppb (33.8% within the GCOS requirements), in spite of the high correlation ($R = 0.937$). This systematic offset is clearly visible in Fig. 4 throughout the whole year. At the Xianghe site, the performance of the OCPR algorithm is better, with 50.0% of the data within the 10ppb GCOS requirement.

The comparison of the GOSAT SRPR product with the TCCON data shows that the RMSE and SD are similar, the correlation R is higher at Hefei than at Xianghe and there are large differences between the bias and the compliance with GCOS requirements. SRPR significantly overestimates XCH_4 in Hefei, with 43.9% of the observations above the GCOS requirements (42.3% within), resulting in a positive bias of +7.229 ppb. In Xianghe the compliance with the GCOS requirements is slightly higher (47.8%), but a large underestimation is observed with 36.3% of the data points below the GCOS requirements and a negative bias of -4.316 ppb.

The evaluation of the GOSAT FOCAL Proxy product shows that more than 50% of the data points meet the GCOS requirements at both sites. However, the short time series provide a limited number of observations that precludes robust statistical results and makes it difficult to effectively neutralize random errors through averaging. This product exhibits the lowest correlation ($R \approx 0.8$) at both sites.

The performance of the GOSAT-2 SRPR is better overall for all four products, with the lowest RMSE (13.2~14.8 ppb) and the highest correlation ($R \approx 0.9$) at both sites. In Hefei, 51.8% of the data points fall within the GCOS target; however, a systematic overestimation is observed at Hefei, with 32.5% of the data pairs above the GCOS requirements and a positive bias of +4.164 ppb. At the Xianghe site 51.3% of the data points meet the GCOS requirements, but 34.4% fall below this range, resulting in a negative bias of -4.968 ppb.

This discussion shows that the performance of GOSAT-2 SRPR is overall better than that of the other three products, with lower bias, RMSE and SD, and 51% within the GCOS requirements which is slightly less than for FOCAL. However, when the matching radius is expanded from ±2.5° to ±5° (Appendix B), its statistical metrics deteriorate significantly (Fig. B2), particularly at the Xianghe site. As illustrated by the spatial distribution maps in Fig. 2 and Fig. A2, the XCH$_4$ exhibits strong spatial variations across the study region. This expanded radius introduces observations from locations farther from the TCCON sites that deviate from the reference levels due to these spatial variations, thereby masking the inherent advantages of the retrieval algorithm at smaller matching scales.

The biases of the four Proxy XCH$_4$ products relative to TCCON observations, averaged in XCH$_4$ bins of 25 ppb, are presented in Fig. 6 as a function of the TCCON-reference XCH$_4$. At the Hefei site, the mean biases of the four Proxy XCH$_4$ products generally exhibit a positive offset, with variations primarily concentrated between 0 and 20 ppb, except for SRPR for which the mean bias is negative in the three largest bins. The biases are largest for the lower XCH$_4$ and overall decreases with increasing XCH$_4$, except for OCPR. The GOSAT FOCAL Proxy (brown) covers a narrower concentration range, with a notable absence of observation data in the low-to-medium range (<1900 ppb); the error bars are significantly larger at the high concentrations, indicating higher retrieval uncertainty. OCPR (blue) shows an overall higher bias, averaging between 10 and 20 ppb. For GOSAT SRPR (orange) the mean bias variations for XCH$_4$ smaller 1900 ppb are similar to those of OCPR, but decreases at higher XCH$_4$ and is negative once concentrations exceed 1975 ppb. The mean bias of the GOSAT-2 SRPR product (magenta) is smaller overall. At high concentrations (>1975 ppb) the mean bias is slightly positive and error bars are small, reflecting high stability and accuracy.

At the Xianghe site the biases are smaller than at Hefei, as indicated above. The mean bias decreases with increasing XCH$_4$ for all products except GOSAT-2 SRPR. OCPR shows the largest positive offset within the low-to-medium concentration range before decreasing toward zero. In contrast, both GOSAT SRPR and the GOSAT FOCAL Proxy decline when XCH$_4$ >1900 ppb, leading to a distinctly negative bias. Conversely, the mean bias of the GOSAT-2 SRPR product is overall slightly negative except in the highest bin where the maximum positive bias is approximately +10 ppb.

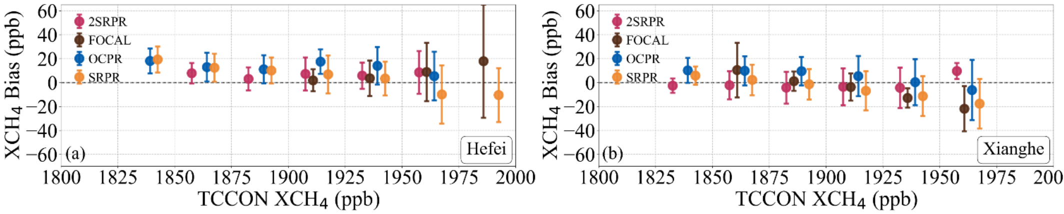

Figure 6. Variation of the mean XCH$_4$ bias, i.e. bias averaged in XCH$_4$ bins with a width of 25 ppb, with TCCON-reference XCH4 for (a) Hefei site; (b) Xianghe site. Error bars indicate the standard deviation of the bias in each bin. The colors indicate the four different proxy algorithms, see legends.

The variations in the biases of the satellite-retrieved XCH$_4$ as function of the TCCON reference XCH$_4$ data during different seasons are presented for the two sites in Fig. 7. The data range varies across seasons, reflecting the higher concentrations in summer and autumn than in winter and spring; notably, the mentioned large variations occur during summer. At the Hefei site (Figs. 7a-d), the positive bias of GOSAT OCPR is most prominent with high values across the entire XCH$_4$ range during spring and summer. The various proxy products show smaller fluctuations of the mean bias among the four data sets during autumn and winter. The only significant divergence appears at high concentrations in autumn, where GOSAT SRPR shows a distinct underestimation, while GOSAT-2 SRPR shows a positive bias.

At the Xianghe site (Fig. 7e-h), GOSAT OCPR shows positive biases in the low-to-medium concentration ranges, while other

https://doi.org/10.5194/egusphere-2026-3382
Preprint. Discussion started: 7 July 2026

products fluctuate around the zero line. Except for GOSAT-2 SRPR, the other products all present a consistent dcrease as XCH_4 increases, manifesting as negative biases at high concentrations. GOSAT-2 SRPR exhibits a slight positive bias in summer and autumn.

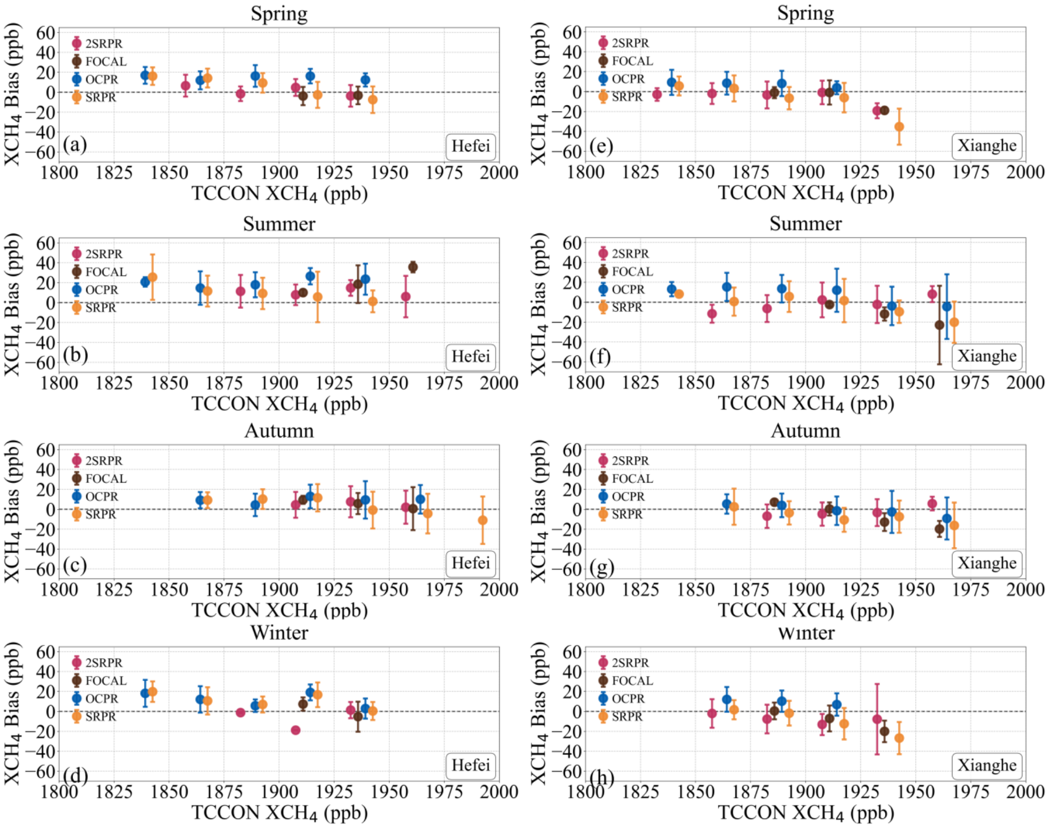

Figure 7. As Fig. 6, but broken down by season, for the Hefei (a) (b) (c) (d) and Xianghe (e) (f) (g) (h) sites. In spring the data are averaged over March, April and May (a, e), in summer over June, July and August (b,f), in autumn over September, October and November (c, g) and in winter over December, January and February (d, h).

The four Proxy products at the Hefei and Xianghe sites are further evaluated through the Taylor diagram plotted in Fig. 8, using the correlation coefficient (R, Eq. (7)), the Centered Root-Mean-Square Error (CRMSE, Eq. (8)) and the Normalized Standard Deviation (NSD, Eq. (9)). The mean bias is excluded from this evaluation to focus on the statistical consistency and precision of the products.

In the Taylor diagram, the distance of the OCPR RMSE to the reference point (star, where R=1 and NSD=1), representing the CRMSE, is relatively small, in spite of having the highest value in Table 3. This confirms that the high OCPR RMSE is primarily driven by systematic bias rather than by random fluctuations. The proximity of the GOSAT-2 SRPR points (circles) at Hefei and Xianghe confirms the robustness and consistency of this algorithm across these two distinct geographical and climatic environments. Furthermore, the CRMSE values for the same algorithms are consistently higher at the Xianghe site than at the Hefei site, except for the GOSAT FOCAL Proxy. This suggests a more pronounced influence of random errors on the total error at Xianghe, thereby complicating the achievement of high retrieval stability. For the GOSAT FOCAL Proxy (squares) precision and stability are lower: it shows the weakest correlation at the both the Hefei and the Xianghe site, whereas at the Hefei site, its NSD significantly exceeds 1.0, reflecting a high degree of data dispersion.

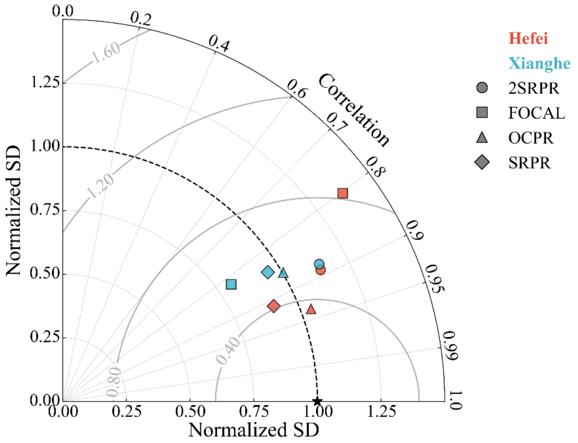

Figure 8. Taylor diagram of CO₂ Proxy XCH₄ products relative to TCCON reference data. Blue and red markers denote the Hefei and Xianghe sites, respectively, with different symbols indicating the XCH₄ proxy products as indicated in the legend. The radial distance from the origin represents the Normalized Standard Deviation (Normalized SD). The azimuthal angle denotes the Correlation Coefficient (R). The Centered Root Mean Square Error (CRMSE) is indicated by the gray dashed concentric semicircles centered at the reference point (the geometric distance to the reference point).

3.2 Validation of XCO_2 estimates used in the proxy algorithms

The four XCO_2 proxy algorithms discussed in this paper use different independent estimates of XCO_2 for the final calculation of XCH_4 (Eq. (1)), based on different models as indicated in the algorithm descriptions. In this Sect., the XCO_2 estimates used in the proxy algorithms are evaluated versus TCCON reference data. For the FOCAL proxy, the XCO_2 estimates are not directly accessible within the satellite products, therefore only the model results for the other three products are validated.

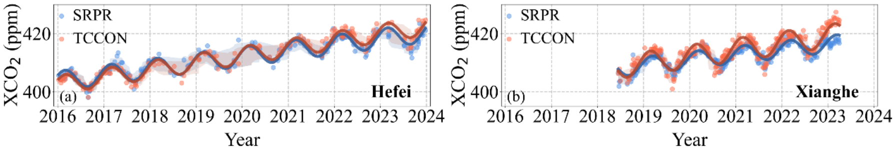

Figure 9. As Fig. 4, but for model XCO_2 data used in GOSAT SRPR XCH_4 retrieval algorithm at the Hefei (a) and the Xianghe (b) sites.

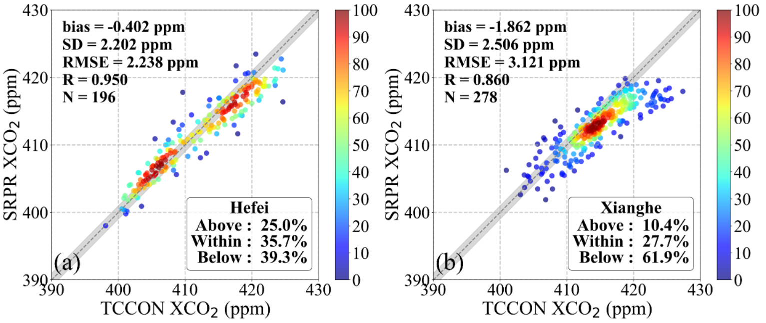

Figure 10. as Fig. 5, but for XCO_2 data retrieved by the GOSAT SRPR XCH_4 retrieval algorithm, at the Hefei (a) and at the Xianghe (b) sites. The grey shaded area indicates an envelope of ±1 ppm, which is consistent with the GCOS precision requirements for XCO_2.

The time series of the model XCO_2 data used in the GOSAT SRPR proxy algorithm is presented in Fig. 9, together with the TCCON XCO_2 data at the Hefei and Xianghe sites. Similar time series for the OCPR and GOSAT-2 SRPR products are presented in Fig. A6 (Appendix A). The time series show seasonal variations similar to those of XCH_4 in Fig. 4, but with a phase

https://doi.org/10.5194/egusphere-2026-3382
Preprint. Discussion started: 7 July 2026

lag of approximately six months. XCO_2 peaks by the end of winter and early spring and minima occur by the end of summer and early autumn. This phase shift is attributed to the asynchronous seasonal variations in the sources and sinks of CH_4 and CO_2: the peak of CH_4 emissions occurs in summer due to vigorous microbial methanogenesis from organic matter decomposition, whereas the peak of CO_2 uptake occurs in summer due to robust photosynthesis, resulting in the observed minimum by the end of summer.

At the Hefei site (Fig. 9a), the uncertainties (shaded areas) for both the SRPR modeled XCO_2 and the TCCON reference data between 2018 and 2021, as well as in early 2023, are much larger than at other times, due to the sparsity of coincident observation points during these periods. The time series show that the model XCO_2 are initially slightly larger than the TCCON observations, whereas in later years the TCCON observations are larger. At the Xianghe site (Fig 9b), the modeled XCO_2 data are noticeably smaller than the TCCON reference data, especially during the spring peaks, with gradually increasing differences toward the end of the time series.

The time series at both TCCON sites show that the evolution of the model XCO_2 resulting in a very pronounced underestimation in early 2023. This is primarily attributable to the sharp surge in emissions driven by the rapid recovery of socio-economic activities in the post-pandemic era (Ahmed and Stern, 2023), which was not captured because the CAMS model values used by the SRPR algorithm only extended to 2015 and were subsequently extrapolated year by year using the 2016 growth rate (3 ppm), rather than reflecting actual emission changes (Wu, 2021a).

The time series observations are confirmed by the scatter density plots of the XCO_2 model data used in the GOSAT SRPR XCH_4 retrieval algorithms versus the TCCON reference data presented in Fig. 10 for both the Hefei and Xianghe sites. Results for other products are presented in Fig. A5 (see Appendix A). The data for the Hefei site (Fig. 10a) show two clusters, one for low XCO_2 (402-409 ppm) where the estimates used in SRPR are slightly overestimated, as in Fig 9a at the beginning of the time series, and one for higher XCO_2 (415 – 421 ppm) where the estimates used in SRPR are underestimated, resulting in an overall bias of -0.40 ppm. At the Xianghe site only one cluster is observed and the model XCO_2 estimates used in SRPR are underestimated resulting in an overall bias of -1.86 ppm. The fraction within the GCOS requirements is low at both sites. The RMSE at the Hefei site (2.24 ppm) is smaller than at the Xianghe site (3.12 ppm). These discrepancies contribute to the uncertainty in the retrieval process.

Density scatterplots for the OCPR and GOSAT-2 SRPR XCH_4 retrieval algorithms and TCCON reference data in Fig. A5 show somewhat different characteristics which vary across algorithms and by site. Like SRPR, OCPR shows two clusters at the Hefei site and a single cluster at the Xianghe site, with a small overestimation in both cases. The GOSAT-2 SRPR algorithm does not show a clear under- or overestimations (Fig. A5b and d), resulting in a small positive bias at Hefei (0.65 ppm) and a small negative bias at Xianghe (-0.70 ppm). The fractions within the GCOS requirements (44.6 % at Hefei and 40.7 % at Xianghe) are larger than for other data products.

3.3 Validation of XCH_4/XCO_2

Time series of the XCH_4/XCO_2 ratios determined using the GOSAT SRPR CO_2 proxy algorithm are presented in Fig. 11, together with ratios determined from the TCCON observations. Results for GOSAT-2 SRPR (2SRPR) and OCPR products are presented in Fig. A6 (see Appendix A). XCH_4/XCO_2 ratios cannot be directly extracted from the FOCAL proxy product datasets. The time series in Figs. 11 and A6 show a distinct seasonal variation with maxima in summer and autumn and minima in winter and spring, similar to the XCH_4 time series in Fig. 3. XCH_4 governs the seasonal variation of the ratio time series because the relative amplitudes for XCH_4 are much larger than for XCO_2. The data in Fig. 11 show that the large uncertainties observed at the Hefei site between 2018 and 2022 are primarily due to the limited number of valid observations during this period.

It is evident that the ratios used in the SRPR XCO_2 proxy algorithm are systematically larger than the ratios derived from the TCCON reference observations. This is also clearly observed in the density scatter plots between the ratios of the retrieval results and the TCCON reference data in Fig. 12. Results for other products are presented in Fig. A7 for both sites separately (see Appendix A). These density scatterplots confirm the substantial and consistent systematic positive biases at both sites, for all three proxy XCH_4 products. The bias at the Hefei site (0.066 ppb/ppm) is somewhat larger than that at the Xianghe site (0.053 ppb/ppm). Despite the systematic overestimation, the SRPR product shows extremely high correlation with the TCCON reference data (R of 0.911 and 0.920, respectively), and its data fluctuation characteristics are highly synchronized with those of the reference data. Furthermore, the data in Fig. A7 show that the OCPR and GOSAT-2 SRPR algorithms are consistent with GOSAT SRPR in terms of retrieval trends and bias characteristics.

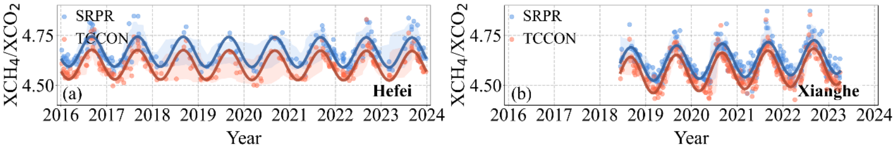

Figure 11. As Fig. 4, but for time series of XCH_4/XCO_2 ratios determined using the GOSAT SRPR CO_2 proxy algorithm at the Hefei (a) and the Xianghe (b) sites.

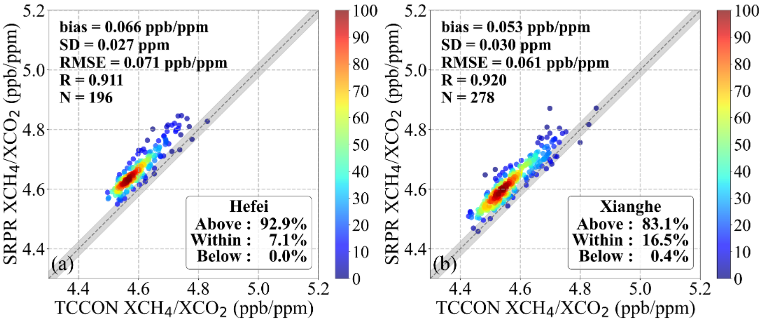

Figure 12. As Fig. 5, but for the XCH_4/XCO_2 ratios determined using the GOSAT SRPR algorithm at the Hefei (a) and the Xianghe (b) sites. The grey shaded area represents an envelope of ±0.025 ppb/ppm, which is derived from the GCOS precision requirements for XCH_4 (10 ppb) and XCO_2 (1 ppm) through the error propagation formula.

In the analysis of the ratios, all proxy XCH_4 products exhibited a pronounced and systematic positive bias across both sites. Consequently, we conducted a separate analysis on the raw XCH_4 and XCO_2 values utilized to compute the ratio; the time series of GOSAT and GOSAT-2 SRPR are presented in Figs. A8 and A9 of Appendix A, while the respective scatterplots are displayed in Figs. A10 and A11. Both GOSAT and GOSAT-2 SRPR raw XCH_4 exhibit a slightly positive bias, which is notably more pronounced at the Xianghe site. For the raw XCO_2 of the GOSAT SRPR product, a systematic negative bias is observed, which gradually decreases in magnitude as TCCON XCO_2 increases. Conversely, GOSAT-2 SRPR exhibits a distinct positive bias that increases with increasing TCCON XCO_2. Furthermore, both satellite generations show a stronger seasonality than the TCCON references across both sites, with large uncertainties. These findings indicate that the persistent overestimation observed in the proxy ratios is predominantly governed by the deviations in raw XCH_4. Consequently, the fundamental assumption underlying the application of the XCO_2 Proxy method—that scattering-induced errors cancel out between the two species—is not fully fulfilled in real-world observations. Hence, empirical post-retrieval corrections based on TCCON observations are indispensable for delivering accurate final products. Additionally, since the raw comparisons reveal a distinct time dependence (as shown in Figs. A8 and A9), the bias corrections must be adjusted and updated regularly.

4 Influence of aerosols on XCH_4

As described in Sect. 2.2, the proxy method is based on the assumption that effects of surface reflectance and aerosols on the

https://doi.org/10.5194/egusphere-2026-3382
Preprint. Discussion started: 7 July 2026

retrieval results are the same for XCH_4 and XCO_2, when these mixing rations are retrieved using the same instrument at the same time and at close wavelengths and thus, cancel out in the ratio XCH_4 / XCO_2 (Barr et al., 2025). The ratio is multiplied with XCO_2 obtained from an independent method to determine the actual XCH_4. However, as shown from the comparison with the TCCON-derived ratio, there is a substantial bias in the SRPR derived ratios at both the Hefei and Xianghe sites (Sect. 3.3). In this section we investigate whether this bias may be caused by a residual influence of aerosols, after filtering the data by using XCO as a tracer to filter out significant anthropogenic pollution events ($\Delta XCO < 36$ ppb) (see Sect. 3). To this end, the bias in the retrieved XCH_4 is evaluated by comparison with AOD at 1640 nm, averaged during ±30 minutes of the satellite overpass. Figure 13 shows the mean bias in XCH_4 retrieved using each of the four proxy algorithms as function of AOD, where the bias is averaged in AOD bins with a bin width of 0.05.

The data in Fig. 13 show the distinct regional differences in bias characteristics relative to AOD between the Hefei and Xianghe sites. At the Hefei site, the mean XCH_4 bias is positive over the whole AOD range, except for two data points where AOD is about 0.4. The bias profile shows a prominent downward curvature, with the mean XCH_4 bias distinctly decreasing as AOD increases up to AOD of 0.2. Within the AOD range of 0.2 – 0.5, the mean XCH_4 bias varies between about -10 ppb and +20 ppb. For AOD > 0.5, the number of retrieval data points is sparse (mainly single retrieval results in each AOD bin and only for GOSAT OCPR and SRPR) with a monotonously increasing bias. In contrast, the bias vs AOD plot for the Xianghe site curves upward, where the bias initially increases with aerosol loading and reaches its maximum at an AOD of approximately 0.23. However, despite this upward trend, the absolute value of the bias at Xianghe is smaller than at Hefei, indicating a higher retrieval accuracy in this region. Other notable differences are observed between the variation with AOD at the two sites. Under low aerosol conditions (AOD < 0.3) at the Xianghe site, GOSAT OCPR shows a systematic positive bias, while SRPR shows a slightly negative bias. The GOSAT-2 SRPR bias at Xianghe varies around -12 ppb for AOD < 0.15, becomes positive (+5 ppb) for larger AOD but for AOD exceeding 0.3 it turns negative again. At the Hefei site, however, the differences in the bias among the 4 products are smaller than at Xianghe, with the smallest value for the GOSAT-2 SRPR bias (close to zero). When AOD exceeds 0.3, the scarcity of valid observation samples leads to a scattered data distribution, making the analysis in high-aerosol environments highly susceptible to individual outliers. Notably, the biases for these high-AOD situations are consistently positive at the Hefei site, whereas at the Xianghe site they are negative.

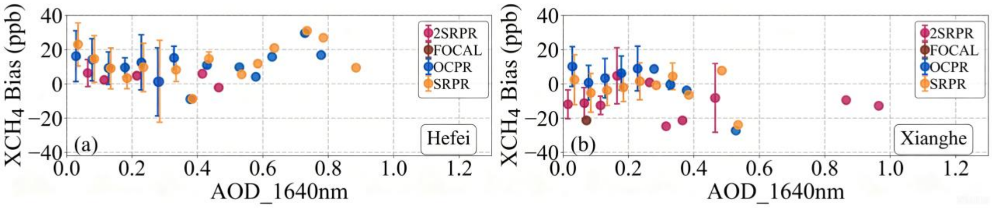

Figure 13. Variation of the mean XCH_4 bias, as function of AOD at 1640 nm, where the bias is averaged in AOD bins with a bin width of 0.05. Error bars indicate the standard deviation in each bin. The XCH_4 bias was determined for each of the four proxy algorithms as indicted in the legend.

5 Discussion

5.1 Time Series Analysis of Bias

Time series of relative bias (defined below, Eq. (11)) for XCH_4, model XCO_2, and the XCH_4/ XCO_2 ratio at the Xianghe site are presented in Fig. 14 and for the Hefei site they are presented in Fig. A12 (Appendix A). The relative XCH_4 bias is defined by Eq. (11):

$$\text{relative bias} = \frac{X_{\text{proxy}} - X_{\text{TCCON}}}{X_{\text{TCCON}}} \times 100\% \qquad (11)$$

where X_{proxy} and X_{TCCON} represent the XCH_4 values retrieved from the satellite and the TCCON ground-based observations, respectively. The relative bias provides a normalized metric to assess the percentage deviation of satellite retrievals from the ground-based benchmark and is used here to facilitate a comparison between the three data products used in the XCH_4 proxy algorithm (Eq. (1)).

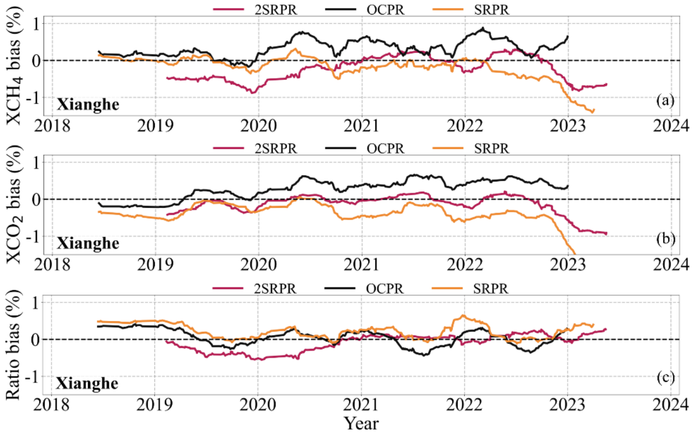

Figure 14. Time series of relative bias for XCH_4 (a), model XCO_2 (b), and the XCH_4/ XCO_2 ratio (c) for the three proxy algorithms at the Xianghe site. Relative bias is calculated following Eq. (11).

Figure 14a shows that the relative bias of the GOSAT OCPR CH_4 product is near zero until 2020, whereafter it varies between 0 and 1% (XCH_4 overestimated). The relative bias of GOSAT SRPR is small and varies around 0 until 2022, when it decreases sharply to smaller than -1% in 2023. The relative bias for GOSAT-2 SRPR is initially negative and gradually increases toward 0 in 2021, and varies around zero before decreasing to negative bias of approximately -1.0% in early 2023. For the model component, Fig. 14b, the XCO_2 relative biases show similar variations across all products, with OCPR overestimating, GOSAT SRPR underestimating, and the GOSAT-2 relative bias varies around zero. Notably, a sudden decrease in the XCO_2 relative bias occurred across all algorithms in late 2022. For ratio, Fig. 14c, the GOSAT SRPR relative bias is positive with variations between 1.0% and 1.5%, which effectively compensates for the negative XCO_2 relative bias in the earlier period resulting in a near-zero relative bias in the final product. The relative bias for the OCPR ratio exhibits frequent random fluctuations (0% to 1.0%), driving the fluctuations of the OCPR XCH_4 retrieval products after 2020. The GOSAT-2 SRPR ratio relative bias was rather small prior to 2021, whereafter it gradually increased to a value of about 0.8% from 2021.

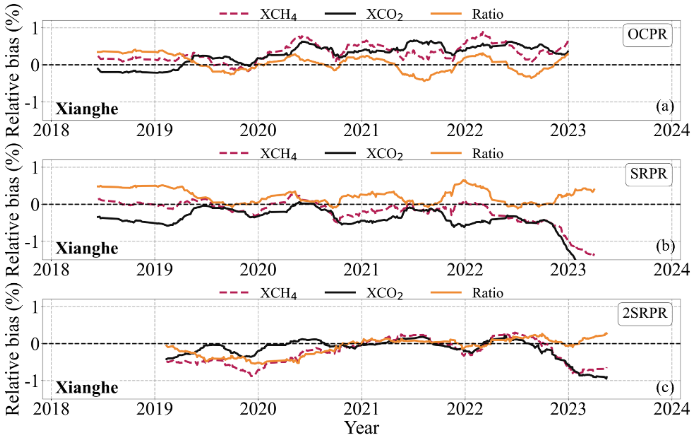

Figure 15. Time series of relative bias for GOSAT OCPR (a), GOSAT SRPR (b), GOSAT-2 SRPR (c) at Xianghe site. Relative bias is calculated using Eq.11.

To further elucidate the origins of the retrieval errors, the contribution of different components to the results from each algorithm is quantitatively assessed using linear decomposition. The time series of relative biases for three products—GOSAT OCPR, GOSAT SRPR, and GOSAT-2 SRPR — at the Xianghe and Hefei sites are presented in Fig. 15 and Fig. A13 (in Appendix A). Using Eq. (1), the impact of each component on the final retrieval accuracy can be quantitatively assessed through the linear decomposition of relative biases:

$$\delta_{\mathrm{XCH_4}} \approx \delta_{\mathrm{XCO_2}} + \delta_{\mathrm{ratio}} \tag{12}$$

where δ_X represents the relative bias of X. Higher-order terms are neglected here. Since the final XCH_4 includes bias correction, the relative bias of XCH_4 is not strictly equal to the sum of relative bias of the two components.

For the OCPR product (Fig. 15a), the fluctuations of the XCH_4 relative bias from mid-2019, are similar to those of the ratio component, indicating that the relative bias trend of the final product from this algorithm is primarily constrained by the fluctuations of the ratio component. In contrast, for the SRPR algorithms (Fig. 15b, c), the variations of the relative bias of XCH_4 trace those of XCO_2; in particular, from mid-2022, the XCH_4 relative bias variations closely follow the sharp fluctuations of XCO_2. Although the relative bias of the final XCH_4 does not strictly equal the algebraic sum of the relative biases of the model XCO_2 and the ratio due to the presence of post-retrieval bias corrections, a distinct offset relationship and mutual compensation can still be observed between them. In the GOSAT SRPR results (Fig. 15b), the relative bias of the ratio component is positive (approximately 1.0% to 1.5%) and, between 2019 and 2022, notably higher than in other algorithms. In contrast, the XCH_4 relative bias was close to zero during this whole period. This indicates that the relative bias of the ratio was effectively compensated by the relative bias of XCO_2. However, after mid-2022, the XCH_4 relative bias was dominated by the strongly decreasing negative relative bias of XCO_2, resulting in a significant decrease of the XCH_4 accuracy. Similarly, for GOSAT-2 SRPR (Fig. 15c), prior to 2021, the smaller magnitude of the ratio's positive correction (with respect to GOSAT SRPR) was insufficient to counteract the negative relative bias of XCO_2, resulting in a negative relative bias for XCH_4. Conversely, after 2021, as the positive relative bias of the ratio increased to approximately 1.0%, better compensation was achieved between the relative biases of ratio and XCO_2, resulting in a nearly zero relative bias of XCH_4. This is mainly because the value of XCO_2 is orders of magnitude larger than that of the ratio, meaning that the final relative bias is predominantly governed by the relative bias of XCO_2.

This decomposition analysis explains the reasons for the discrepancies between the CO_2 Proxy method derived XCH_4 accuracies at the Hefei and Xianghe sites observed in Sect. 3.1. The XCH_4 accuracy is primarily determined by the a priori XCO_2 model. At the Hefei site, the model XCO_2 exhibits a generally positive relative bias, leading to an overestimation across the final XCH_4 products. In contrast, at the Xianghe site, the relative bias of model XCO_2 is negative, except for the OCPR algorithm.

5.2 Spatial Analysis of Bias

As analyzed in Sect. 3.1, extending the spatial domain to a broader ±5° spatial extent introduces substantial spatial variation, and therefore we adopted a ±2.5° spatial extent. While Table 3 provides the mean bias averaged over the ±2.5° validation area, spatial variability may still persist inside this spatial extent. Therefore, the influence of this localized spatial variation within the selected spatial extent on the overall comparison results was evaluated. In this study, the study area was partitioned into 0.1° × 0.1° latitude-longitude grids. Individual residuals, obtained by subtracting the corresponding TCCON measurements from each matched satellite observation, were projected into the grid cells based on their geographic coordinates. To eliminate random noise from individual observations and represent the overall bias level of the region, the median value of all matched data point residuals within a single grid cell was calculated as the representative value for that grid cell. These values were then plotted using a color scale representing the XCH_4 bias. The spatial distributions of the biases for the four XCH_4 products at the Xianghe site are presented in Fig. 16, and for the Hefei site in Fig. A14 (Appendix A).

The data in Fig. 16a show the occurrence of the largest positive biases for the OCPR XCH_4 product around the Xianghe site and especially to the south, with median values ranging between +10 and +30 ppb. While Table 3 provides an overall mean bias of 6.3 ppb for the validation area, Fig. 16a demonstrates that this single statistical value masks significant intra-region variability. Specifically, the strong overestimation over the southern regions is partially offset by the negative biases distributed across the northern parts of the domain. The GOSAT SRPR XCH_4 bias is generally negative near the site but transitions to overestimation in the southern region. The GOSAT-2 SRPR XCH_4 product around Xianghe is distributed over a closer range to the TCCON site, with an overall negative bias. The data coverage of the GOSAT FOCAL Proxy XCH_4 product is sparse and generally shows a negative bias to the northwest of the site, while to the southwest the biases are mostly positive. The distinct spatial heterogeneities and the shift toward positive biases observed in the southern areas across these products are likely due to the strong spatial gradients of XCH_4. This spatial discrepancy primarily reflects the inherent representation errors between the localized TCCON point measurements and the larger footprints of satellite observations within the matching domain. Notably, the spatial consistency of the GOSAT-2 product is significantly improved compared to the other GOSAT products. As detailed in Sect. 2.3.2, the GOSAT-2 b parameter (0.00158) is smaller, which minimizes the influence of surface albedo variations on XCH_4 retrieval results.

Similar plots of the spatial variation of the biases at the Hefei site are presented in Fig. A14. These data show that positive biases dominate in the inland areas to the west of the site, whereas slightly negative biases are found in the coastal regions to the northeast.

Statistical analysis in Sect. 3.1 reveals a significant systematic discrepancy in XCH_4 retrieval biases between the two sites: a prevalent overestimation at the Hefei site and a general underestimation at the Xianghe site (with the exception of OCPR). Given its proximity to anthropogenic emission sources in the North China Plain, the TCCON measurements at Xianghe likely exceed the regional background levels captured by satellite sampling (Yang et al., 2020), leading to a negative offset. At the Hefei site, the satellite tracks primarily pass over the western inland areas, where methane concentrations are relatively high (Fig. 2). Due to this geographic offset, satellite observations capture the higher concentrations to the west rather than matching the local TCCON reference levels, leading to an overestimation.

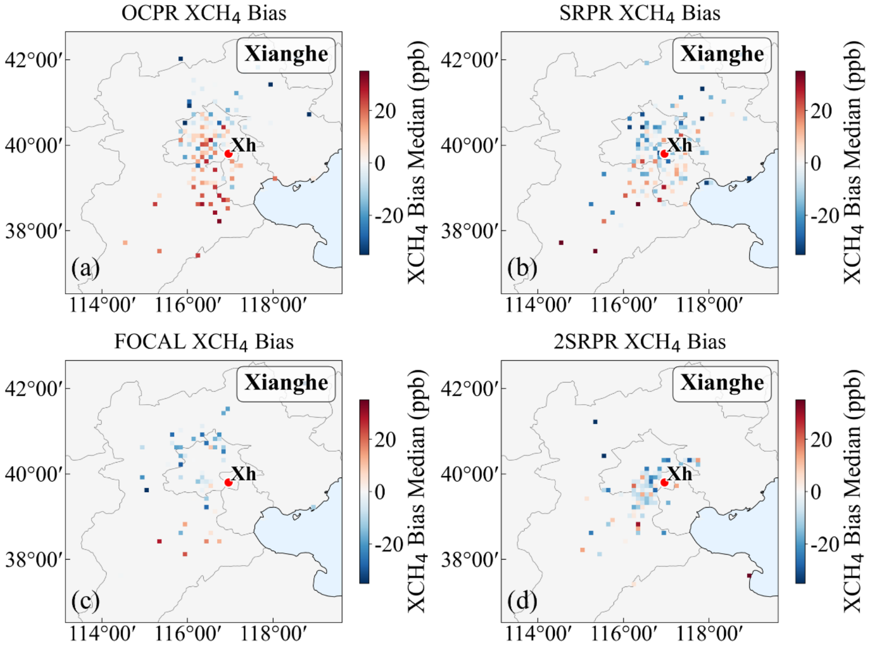

Figure 16. Spatial variation of the median XCH_4 biases (see text for explanation) around the Xianghe site on a 0.1 by 0.1° latitude-longitude grid.

6 Conclusions

Four Proxy XCH_4 satellite retrieval products (GOSAT OCPR, SRPR, FOCAL Proxy, and GOSAT-2 SRPR) were evaluated using ground-based observation data from the TCCON sites in Hefei and Xianghe, China. All products effectively captured the long-term increase of XCH_4 in China and the distinct seasonal cycles (maxima in summer/autumn and minima in spring/winter). Spatially, they consistently captured the distinct south-to-north and east-to-west variations, showing a prominent 'high in the southeast and low in the northwest' pattern.

In terms of site-specific validation, the performance of the GOSAT products (OCPR, SRPR, FOCAL Proxy) is better at Xianghe, whereas the GOSAT-2 SRPR product exhibits comparable performance across both sites. GOSAT OCPR shows the most severe systematic overestimation at the Hefei site (bias of +13.197 ppb), with high correlation (R=0.937) but only 33.8% of the data meeting the GCOS requirements and 62.1% above. GOSAT SRPR has a positive bias (+7.229 ppb, 43.9% exceeding the GCOS upper limit of +10%) and a negative bias (-4.316 ppb) at the Xianghe site. Although the GOSAT FOCAL Proxy performs relatively well in the low-to-medium concentration range (>50% meeting GCOS requirements at both sites), it is constrained by a limited sample size, leading to larger error bars at high concentrations. GOSAT-2 SRPR shows the lowest RMSE (13.2~14.8 ppb) and the highest correlation ($R \approx 0.9$) at both sites, with 51.8% and 51.3% of the data within the GCOS target range. Despite a positive offset of approximately +10 ppb at high concentrations (>1975 ppb), its error bars remain small, reflecting high stability. However, when the matching radius is expanded to ±5°, the statistical performance at the Xianghe site deteriorates significantly with extreme outliers. This degradation is primarily because the larger window introduces data points further away that deviate from the TCCON reference due to regional spatial variation. Consequently, the advanced pointing capability of GOSAT-2 provides a larger volume of high-quality data, which allows for more stringent spatial matching criteria in ground validation while still maintaining a statistically reliable sample size.

Component decomposition reveals that while total bias across all products results from the combined effects of the offsets of the XCH_4/XCO_2 ratio and the XCO_2 prior, the primary drivers of their variations are different. Fluctuations of the OCPR bias are similar to those of the ratio, whereas the bias fluctuations of the SRPR series (including GOSAT and GOSAT-2) is governed by the XCO_2 prior. The contributions from different factors in the Proxy method explain the polarity of XCH_4 biases between sites; the overestimation at Hefei and the general underestimation at Xianghe (except for OCPR) are primarily determined by the performance of the XCO_2 prior model at the two locations. Analysis of raw constituents indicates that the ratio overestimation is primarily driven by the positive bias in raw XCH_4, while raw XCO_2 exhibits systematic biases (negative for GOSAT, decreasing with concentration; positive for GOSAT-2, increasing with concentration). This demonstrates that the proxy method's error-cancellation assumption is not fully fulfilled, necessitating experimental post-retrieval corrections. The spatial analysis further indicates that these discrepancies are also driven by the spatial inconsistency between satellite and ground-based measurements. At the Hefei site, the satellite tracks pass over areas with high methane concentrations to the west of the site, leading to the occurrence of positive bias. At the Xianghe site, TCCON point measurements are significantly higher than the regional background captured by satellite footprints, leading to a systematic underestimation.

The influence of aerosols on the retrieval results should be eliminated by using the CO_2 Proxy method. However, the evaluation of the influence of AOD (at 1640 nm) shows the occurrence of an AOD-dependent bias at both sites, but with distinctly different effects. At the Hefei site, the bias first decreases for AOD up to about 0.4 then increases, whereas, at the Xianghe site the variation of the XCH_4 bias with AOD is opposite. The bias at the Xianghe site is lower than that at the Hefei site. Furthermore, the GOSAT-2 SRPR products show high stability under low aerosol concentrations at both sites; it shows minor fluctuations around zero at Hefei, whereas at the Xianghe site the bias is approximately -12 ppb.

Overall, GOSAT-2 SRPR provides the highest accuracy and correlation under stringent spatial matching conditions, making it the preferred choice for refined regional monitoring and “Dual Carbon” goal accounting. GOSAT OCPR exhibits a notable systematic positive offset, it effectively captures consistent spatiotemporal trends and can serve as a reference for long-term dynamic analysis. However, in practical applications, the limitations of this method must be fully considered. The core assumption of the XCO_2 Proxy method—namely, that scattering-induced errors can be synchronously canceled out—is not fully fulfilled; the persistent overestimation in proxy ratios is predominantly driven by the positive bias in raw XCH_4. Furthermore, the evaluation of AOD effects reveals significant, site-specific residual biases, directly demonstrating that the method's ability to eliminate aerosol-induced errors is limited. Therefore, empirical corrections are strictly required and must be adjusted and updated regularly due to the distinct time dependence observed in the raw biases. Since the accuracy of Proxy products is inherently constrained by the XCO_2 prior model accuracy, future applications should prioritize differential bias correction schemes for different climate zones and improve the spatiotemporal resolution and local emission representation of prior models in high-emission regions, thereby providing more reliable data support for refined methane monitoring in China.

Appendix A: Supplementary Validation Results

Appendix A provides figures supplementary to those in the main text, offering a comprehensive evaluation of the retrieval performance for the four products across both site environments while limiting the number of similar figures.

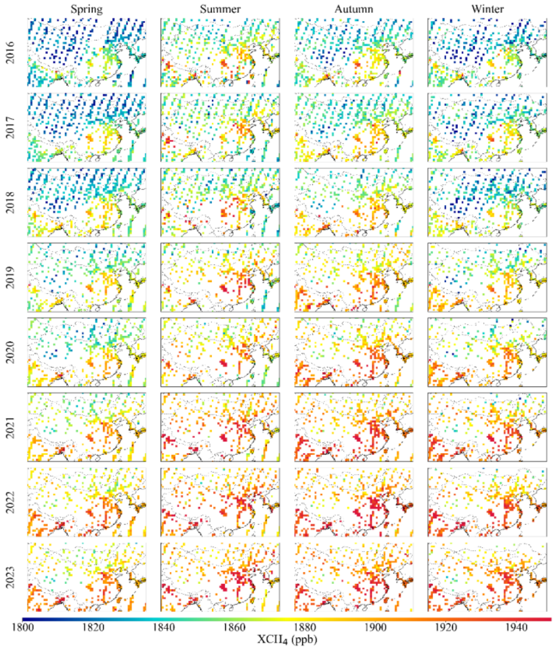

Figure A1. Maps of seasonal mean GOSAT SRPR XCH_4 for the years 2016–2023.

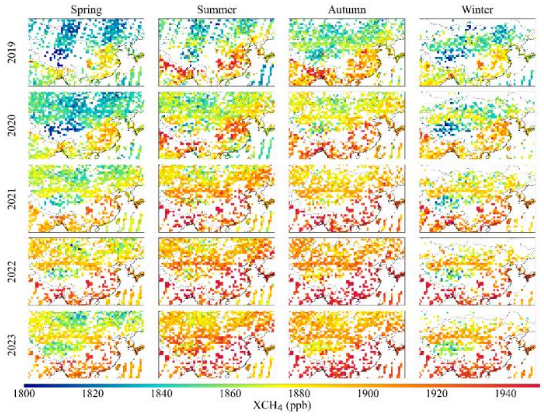

Figure A2. Maps of seasonal mean GOSAT-2 SRPR XCH_4 for the years 2019–2023.

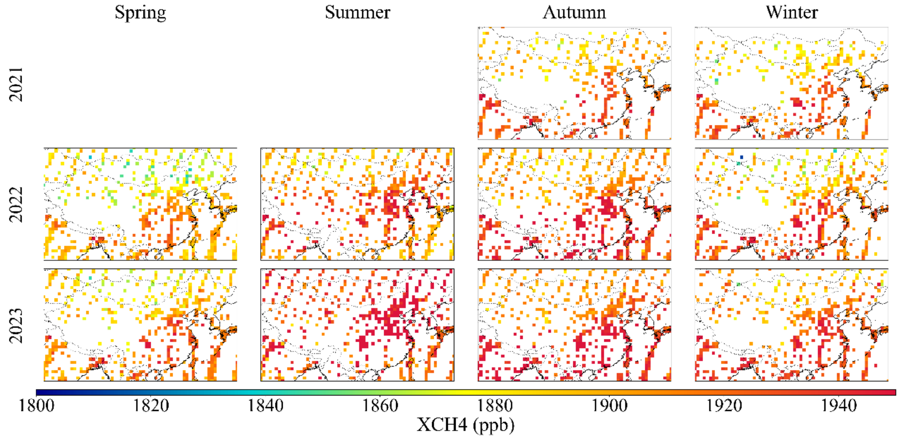

Figure A3. Maps of seasonal mean GOSAT FOCAL Proxy XCH₄ for the years 2021–2023.

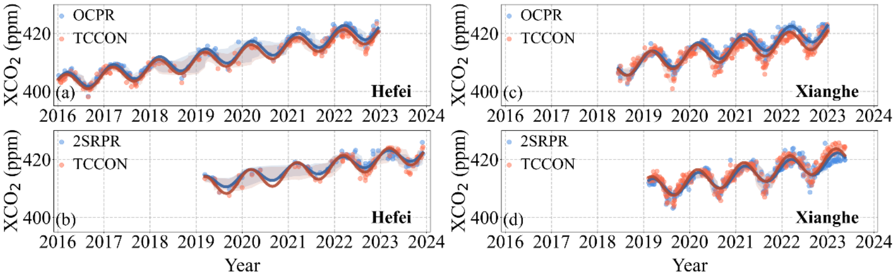

Figure A4. As Fig. 4, but for model XCO_2 data used in GOSAT OCPR and GOSAT-2 SRPR XCH_4 retrieval algorithms (see text), compared with TCCON data over Hefei (a) (b) and Xianghe (c) (d) sites.

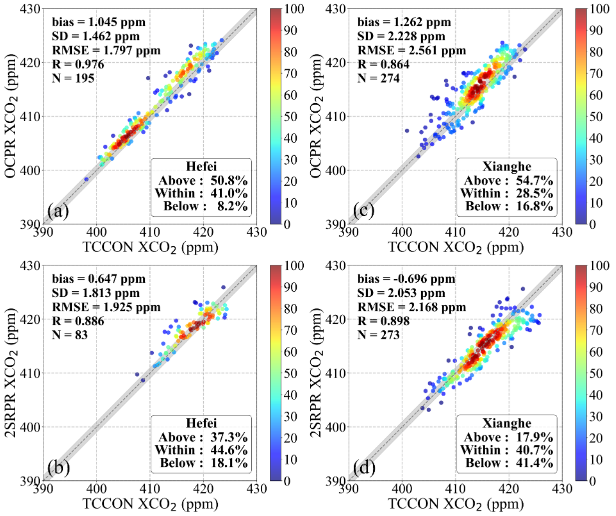

Figure A5. As Fig. 5, but for XCO_2 model data retrieved by the GOSAT OCPR and GOSAT-2 SRPR XCH_4 retrieval algorithms for the Hefei (a) (c) and Xianghe (b) (d) sites.

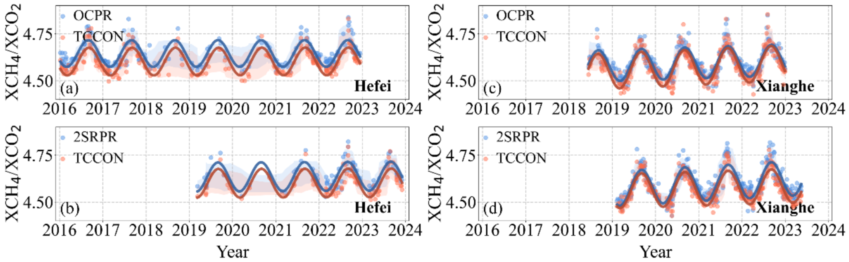

Figure A6. As Fig. 4, but for XCH_4/XCO_2 ratios determined using the GOSAT OCPR and GOSAT-2 SRPR XCH_4 retrieval algorithms.

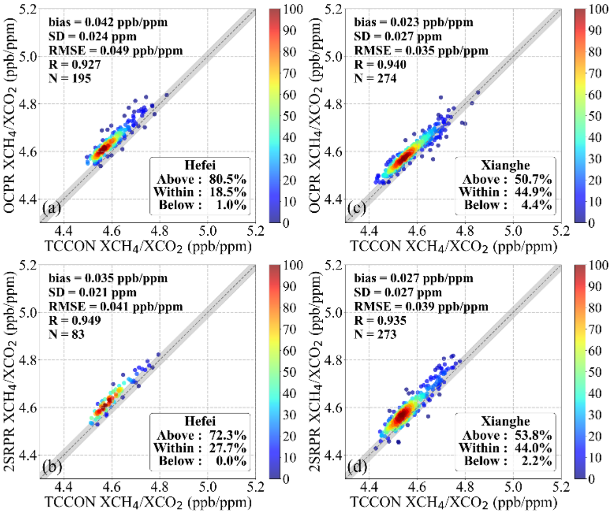

Figure A7. As Fig. 5, but for XCH_4/XCO_2 ratios determined using the GOSAT OCPR and GOSAT-2 SRPR XCH_4 retrieval algorithms for Hefei (a) (c) and Xianghe (b) (d).

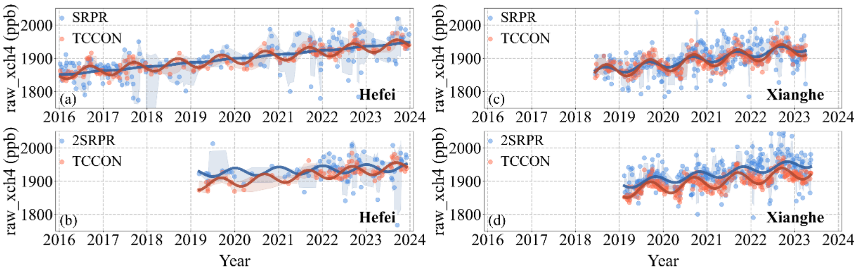

Figure A8. As Fig. 4, but for the raw XCH_4 used to calculate the ratios for the SRPR retrieval algorithms.

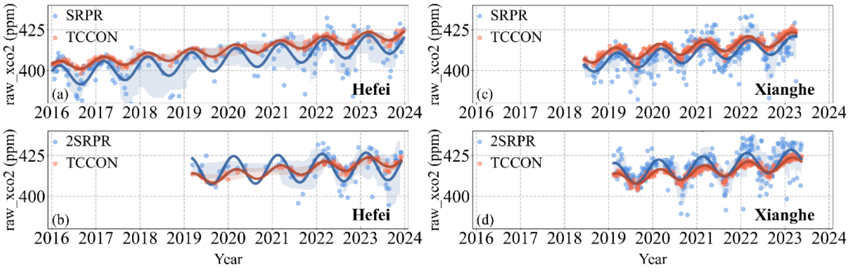

Figure A9. As Fig. 4, but for the raw XCO_2 used to calculate the ratios for the SRPR retrieval algorithms.

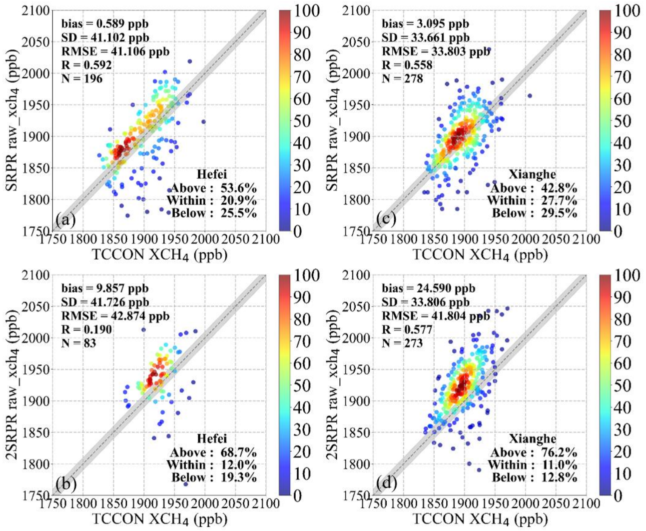

Figure A10. As Fig. 5, but for the raw XCH₄ used to calculate the ratios for the SRPR retrieval algorithms.

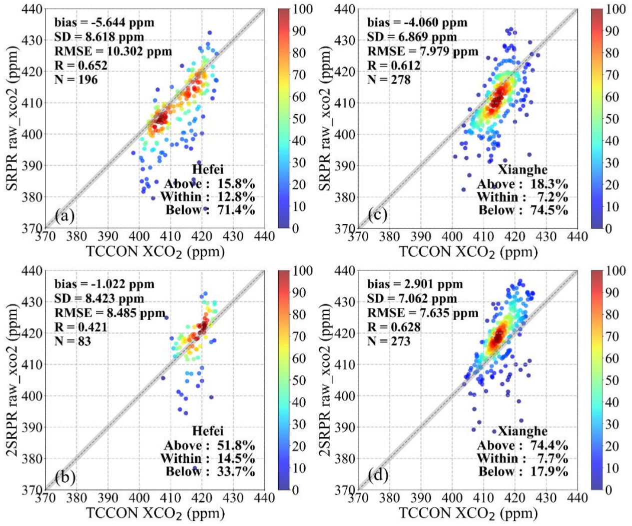

Figure A11. As Fig. 5, but for the raw XCO₂ used to calculate the ratios for the SRPR retrieval algorithms.

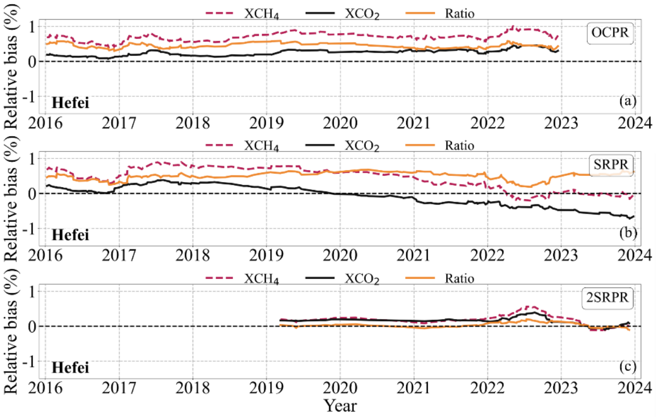

Figure A12. As Fig. 14, but for Hefei site.

https://doi.org/10.5194/egusphere-2026-3382
Preprint. Discussion started: 7 July 2026

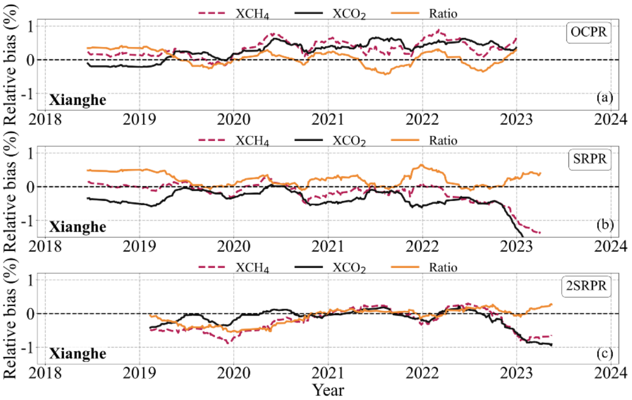

Figure A13. As Fig. 15, but for Hefei site.

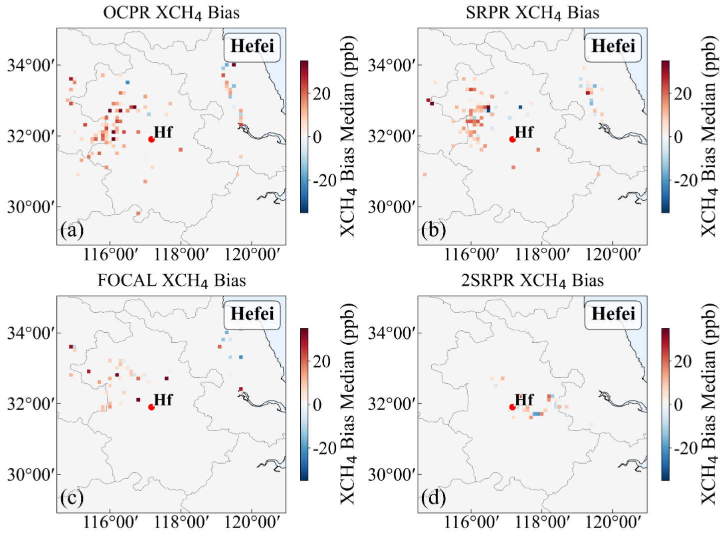

Figure A14. As Fig. 16, but for Hefei site.

Appendix B: Results from Alternative Matching Schemes

In addition to the spatial matching scheme using in the main text (with data averaged within a ±2.5° spatial window, also a broader spatial matching scheme has been incorporated with GOSAT and GOSAT-2 observations averaged within a ±5° spatial window centered at each TCCON station. For each satellite overpass, a spatial representative value was derived by averaging all valid pixels within this window. TCCON measurements were averaged within a ±2-hour window relative to the satellite overpass time, thereby accounting for short-term atmospheric variability. Final data pairs were strictly filtered to retain only those instances where valid satellite and ground-based measurements co-existed within these defined spatiotemporal windows. The validation results are shown in Figs. B1-B4.

https://doi.org/10.5194/egusphere-2026-3382
Preprint. Discussion started: 7 July 2026

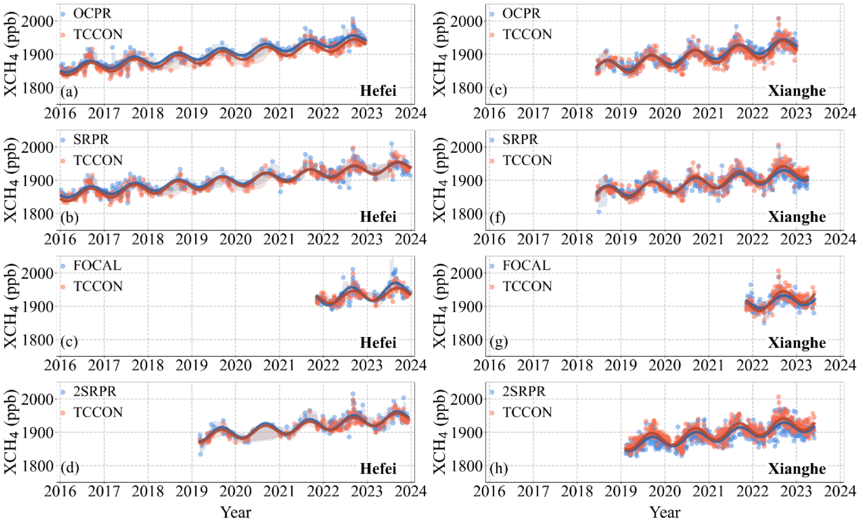

Figure B1. As Fig. 4, but for the ±5° spatial matching condition.

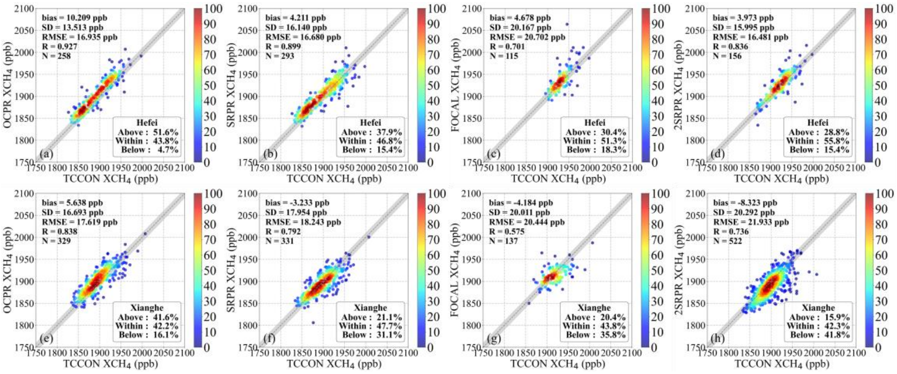

Figure B2. As Fig. 5, but for the ±5° spatial matching condition.

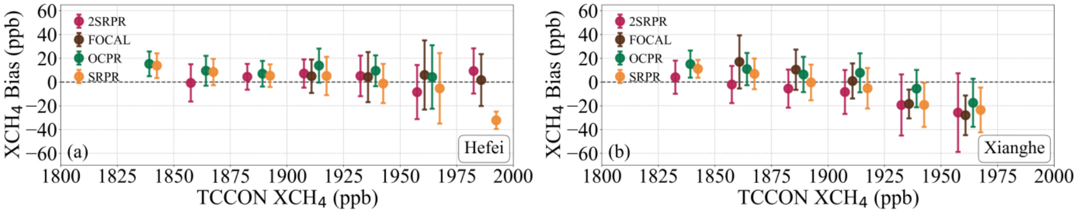

Figure B3. As Fig. 6, but for the ±5° spatial matching condition.

Data availability

The GOSAT OCPR XCH₄ (v9.0), GOSAT SRPR XCH₄ (v2.3.9), and GOSAT-2 SRPR XCH₄ (v2.0.1) datasets used in this study were obtained from the Copernicus Climate Data Store (CDS) (https://cds.climate.copernicus.eu/datasets/satellite-methane?tab=download). The GOSAT FOCAL Proxy XCH₄ (v3.0) data product was sourced from the University of Bremen, Institute of Environmental Physics (IUP), Carbon and Greenhouse Gas Group (https://www.iup.uni-bremen.de/~ghguser/gosat_focal/NRT_v3.0/data/).

The TCCON data are available at https://tccondata.org/. This study utilizes the GGG2020 release for both sites. The specific datasets are available via their respective DOIs: https://doi.org/10.14291/tccon.ggg2020.hefei01.R1 (Hefei) and https://doi.org/10.14291/tccon.ggg2020.xianghe01.R0 (Xianghe).

The AERONET data are available at https://aeronet.gsfc.nasa.gov/. And the SONET data are made available by request through a data use agreement and application form with Dr. Li Li (email: lili3@radi.ac.cn).

Author contributions

All authors contributed to the study's conception and design. Xinran Jiang performed the experiments and wrote the original draft of the manuscript. Gerrit de Leeuw and Cheng Fan provided guidance on research design. Gerrit de Leeuw, Cheng Fan, Jeon-Teo Dong, and Zhengqiang Li contributed to the review, commentary, revision of the manuscript and finalized it. All authors read, reviewed, and approved the final manuscript.

Competing interests

The authors declare that they have no conflict of interest.

Disclaimer

Acknowledgements

The study contributes to the ESA/MOST cooperation project Dragon 6 "Air Quality Monitoring and Analysis in Populous areas in China" (AQMAP).
The TCCON data were obtained from the TCCON Data Archive hosted by CaltechDATA at https://tccondata.org/. We thank the TCCON community for providing the ground-based remote sensing data used in this study.

Financial support

This work was supported by the Jing-Jin-Ji Regional Integrated Environmental Improvement-National Science, the Technology Major Project of Ministry of Ecology and Environment of China (Grant No. 2025ZD1200900), the Chinese Academy of Sciences President's International Fellowship Initiative (Grant No. 2025PVA0014_Y1).

References

Agustí-Panareda, A., Barré, J., Massart, S., Inness, A., Aben, I., Ades, M., Baier, B. C., Balsamo, G., Borsdorff, T., Bousserez, N., Boussetta, S., Buchwitz, M., Cantarello, L., Crevoisier, C., Engelen, R., Eskes, H., Flemming, J., Garrigues, S., Hasekamp, O., Huijnen, V., Jones, L., Kipling, Z., Langerock, B., McNorton, J., Meilhac, N., Noël, S., Parrington, M., Peuch, V. H., Ramonet, M., Razinger, M., Reuter, M., Ribas, R., Suttie, M., Sweeney, C., Tarniewicz, J., and Wu, L.: Technical note: The CAMS greenhouse gas reanalysis from 2003 to 2020, Atmos. Chem. Phys., 23, 3829–3859, https://doi.org/10.5194/acp-23-3829-2023, 2023.
Ahmed, K. and Stern, D. I.: China's carbon emissions trend after the pandemic, Environmental Challenges, 13, 100787, https://doi.org/10.1016/j.envc.2023.100787, 2023.
Alvarez, R. A., Zavala-Araiza, D., Lyon, D. R., Allen, D. T., Barkley, Z. R., Brandt, A. R., Davis, K. J., Herndon, S. C., Jacob, D. J., Karion, A., Kort, E. A., Lamb, B. K., Lauvaux, T., Maasakkers, J. D., Marchese, A. J., Omara, M., Pacala, S. W., Peischl, J., Robinson, A. L., Shepson, P. B., Sweeney, C., Townsend-Small, A., Wofsy, S. C., and Hamburg, S. P.: Assessment of methane emissions from the U.S. oil and gas supply chain, Science, 361, 186–188, https://doi.org/10.1126/science.aar7204, 2018.

Andrey, B., Sergey, O., Tatsuya, Y., Yukio, Y., Isamu, M., Osamu, U., Dmitry, B., and Shamil, M.: Retrievals of atmospheric CO2, CH4 and optical path modifications from the GOSAT observations, Proc.SPIE, in: Remote Sensing of Clouds and the Atmosphere XVIII; and Optics in Atmospheric Propagation and Adaptive Systems XVI, 17 Octorber 2013, 889008, https://doi.org/10.1117/12.2028486, 2013.

Barr, A. and Borsdorff, T.: Product User Guide and Specification (PUGS) – ANNEX C for product CH4_GO2_SRPR (v2.0.1, 2019-2022), SRON Netherlands Institute for Space Research, Netherlands, 2023.

Barr, A. G., Schneising, O., and Heymann, J.: Algorithm Theoretical Basis Document (ATBD) - ANNEX C for product CH4_GO2_SRPR (v2.0.1, 2019-2022), SRON Netherlands Institute for Space Research, Bremen, 2023.

Barr, A. G., Landgraf, J., Martinez-Velarte, M., Vrekoussis, M., Sussmann, R., Morino, I., Strong, K., Zhou, M., Velazco, V. A., Ohyama, H., Warneke, T., Hase, F., and Borsdorff, T.: Five years of GOSAT-2 retrievals with RemoTeC: XCO2 and XCH4 data products with quality filtering by machine learning, Atmos. Meas. Tech., 18, 6093–6123, https://doi.org/10.5194/amt-18-6093-2025, 2025.

Bey, I., Jacob, D. J., Yantosca, R. M., Logan, J. A., Field, B. D., Fiore, A. M., Li, Q., Liu, H. Y., Mickley, L. J., and Schultz, M. G.: Global modeling of tropospheric chemistry with assimilated meteorology: Model description and evaluation, Journal of Geophysical Research: Atmospheres, 106, 23073–23095, https://doi.org/10.1029/2001JD000807, 2001.

Boesch, H. and Di Noia, A.: Product User Guide and Specification (PUGS) – ANNEX A for products CO2_GOS_OCFP, CH4_GOS_OCFP (v7.3, 2009-2021) & CH4_GOS_OCPR (v9.0, 2009-2021), University of Bremen, Bremen, 2023.

Boesch, H., Anand, J., and Di Noia, A.: Algorithm Theoretical Basis Document (ATBD) – ANNEX A for products CO2_GOS_OCFP (v7.3), CH4_GOS_OCFP (v7.3) & CH4_GOS_OCPR (v9.0) (CDR7, 2009-2022), University of Bremen, BremenC3S2_312a_Lot2-WP2_PUGS- 2022- GHG_ANNEX- A_v7.2, 2024.

Bovensmann, H., Burrows, J. P., Buchwitz, M., Frerick, J., Noël, S., Rozanov, V. V., Chance, K. V., and Goede, A. P. H.: SCIAMACHY: Mission Objectives and Measurement Modes, Journal of the Atmospheric Sciences, 56, 127–150, https://doi.org/10.1175/1520-0469(1999)056<0127:SMOAMM>2.0.CO;2, 1999.

Buchwitz, M., Rozanov, V. V., and Burrows, J. P.: A near-infrared optimized DOAS method for the fast global retrieval of atmospheric CH4, CO, CO2, H2O, and N2O total column amounts from SCIAMACHY Envisat-1 nadir radiances, Journal of Geophysical Research: Atmospheres, 105, 15231–15245, https://doi.org/10.1029/2000JD900191, 2000.

Buchwitz, M., Schneising, O., Reuter, M., Heymann, J., Krautwurst, S., Bovensmann, H., Burrows, J. P., Boesch, H., Parker, R. J., Somkuti, P., Detmers, R. G., Hasekamp, O. P., Aben, I., Butz, A., Frankenberg, C., and Turner, A. J.: Satellite-derived methane hotspot emission estimates using a fast data-driven method, Atmos. Chem. Phys., 17, 5751–5774, https://doi.org/10.5194/acp-17-5751-2017, 2017.

Butz, A., Hasekamp, O. P., Frankenberg, C., and Aben, I.: Retrievals of atmospheric CO2 from simulated space-borne measurements of backscattered near-infrared sunlight: accounting for aerosol effects, Appl. Opt., 48, 3322–3336, https://doi.org/10.1364/AO.48.003322, 2009.

Butz, A., Hasekamp, O. P., Frankenberg, C., Vidot, J., and Aben, I.: CH4 retrievals from space-based solar backscatter measurements: Performance evaluation against simulated aerosol and cirrus loaded scenes, Journal of Geophysical Research: Atmospheres, 115, https://doi.org/10.1029/2010JD014514, 2010.

Butz, A., Guerlet, S., Hasekamp, O., Schepers, D., Galli, A., Aben, I., Frankenberg, C., Hartmann, J. M., Tran, H., Kuze, A., Keppel-Aleks, G., Toon, G., Wunch, D., Wennberg, P., Deutscher, N., Griffith, D., Macatangay, R., Messerschmidt, J., Notholt, J., and Warneke, T.: Toward accurate CO2 and CH4 observations from GOSAT, Geophysical Research Letters, 38, https://doi.org/10.1029/2011GL047888, 2011.

Chevallier, F., Feng, L., Bösch, H., Palmer, P. I., and Rayner, P. J.: On the impact of transport model errors for the estimation of CO2 surface fluxes from GOSAT observations, Geophysical Research Letters, 37, https://doi.org/10.1029/2010GL044652, 2010.

Costantiello, A., Laureti, L., Quarto, A., and Leogrande, A.: Methane Emissions in the ESG Framework at the World Level, https://doi.org/10.3390/methane4010003, 2025.

East, J. D., Jacob, D. J., Balasus, N., Bloom, A. A., Bruhwiler, L., Chen, Z., Kaplan, J. O., Mickley, L. J., Mooring, T. A., Penn, E., Poulter, B., Sulprizio, M. P., Worden, J. R., Yantosca, R. M., and Zhang, Z.: Interpreting the Seasonality of Atmospheric Methane, Geophysical Research Letters, 51, e2024GL108494, https://doi.org/10.1029/2024GL108494, 2024.

GOSAT-2 (Greenhouse gases Observing Satellite-2) / Ibuki-2: https://www.eoportal.org/satellite-missions/gosat-2, last access: 28 May 2026, 2024 2026, 2024.

GCOS: The 2022 GCOS ECVs Requirements, World Meteorological Organization, Geneva, SwitzerlandGCOS-245, https://library.wmo.int/doc_num.php?explnum_id=11318, 2022.

Hansen, J. E. and Sato, M.: Trends of measured climate forcing agents, Proceedings of the National Academy of Sciences, 98, 14778–14783, 10.1073/pnas.261553698, 2001.

Holben, B. N., Eck, T. F., Slutsker, I., Tanré, D., Buis, J. P., Setzer, A., Vermote, E., Reagan, J. A., Kaufman, Y. J., Nakajima, T., Lavenu, F., Jankowiak, I., and Smirnov, A.: AERONET—A Federated Instrument Network and Data Archive for Aerosol Characterization, Remote Sensing of Environment, 66, 1–16, https://doi.org/10.1016/s0034-4257(98)00031-5, 1998.

Holben, B. N., Tanré, D., Smirnov, A., Eck, T. F., Slutsker, I., Abuhassan, N., Newcomb, W. W., Schafer, J. S., Chatenet, B., Lavenu, F., Kaufman, Y. J., Castle, J. V., Setzer, A., Markham, B., Clark, D., Frouin, R., Halthore, R., Karneli, A., O'Neill, N. T., Pietras, C., Pinker, R. T., Voss, K., and Zibordi, G.: An emerging ground-based aerosol climatology: Aerosol optical depth from AERONET, Journal of Geophysical Research: Atmospheres, 106, 12067–12097, https://doi.org/10.1029/2001JD900014, 2001.

Hong, X., Gao, Y., Wang, J., Zhang, C., Chen, H., Ni, Y., Wang, W., Sun, Y., Zhu, Y., Tang, Z., Wang, Y., Ma, N., and Liu, C.: Evaluating the performance of carbon dioxide and methane observations from carbon-monitoring satellite products over China, Science of The Total Environment, 955, 176896, https://doi.org/10.1016/j.scitotenv.2024.176896, 2024.

Hourdin, F., Musat, I., Bony, S., Braconnot, P., Codron, F., Dufresne, J.-L., Fairhead, L., Filiberti, M.-A., Friedlingstein, P., Grandpeix, J.-Y., Krinner, G., LeVan, P., Li, Z.-X., and Lott, F.: The LMDZ4 general circulation model: climate performance and sensitivity to parametrized physics with emphasis on tropical convection, Climate Dynamics, 27, 787–813, https://doi.org/10.1007/s00382-006-0158-0, 2006.

Hu, H., Hasekamp, O., Butz, A., Galli, A., Landgraf, J., Aan de Brugh, J., Borsdorff, T., Scheepmaker, R., and Aben, I.: The operational methane retrieval algorithm for TROPOMI, Atmos. Meas. Tech., 9, 5423–5440, https://doi.org/10.5194/amt-9-5423-2016, 2016.

Imasu, R., Matsunaga, T., Nakajima, M., Yoshida, Y., Shiomi, K., Morino, I., Saitoh, N., Niwa, Y., Someya, Y., Oishi, Y., Hashimoto, M., Noda, H., Hikosaka, K., Uchino, O., Maksyutov, S., Takagi, H., Ishida, H., Nakajima, T. Y., Nakajima, T., and Shi, C.: Greenhouse gases Observing SATellite 2 (GOSAT-2): mission overview, Progress in Earth and Planetary Science, 10, 33, https://doi.org/10.1186/s40645-023-00562-2, 2023.

Inness, A., Baier, F., Benedetti, A., Bouarar, I., Chabrillat, S., Clark, H., Clerbaux, C., Coheur, P., Engelen, R. J., Errera, Q., Flemming, J., George, M., Granier, C., Hadji-Lazaro, J., Huijnen, V., Hurtmans, D., Jones, L., Kaiser, J. W., Kapsomenakis, J., Lefever, K., Leitão, J., Razinger, M., Richter, A., Schultz, M. G., Simmons, A. J., Suttie, M., Stein, O., Thépaut, J. N., Thouret, V., Vrekoussis, M., Zerefos, C., and the, M. t.: The MACC reanalysis: an 8 yr data set of atmospheric composition, Atmos. Chem. Phys., 13, 4073–4109, https://doi.org/10.5194/acp-13-4073-2013, 2013.

IPCC: Climate Change 2021: The Physical Science Basis. Contribution of Working Group I to the Sixth Assessment Report of the Intergovernmental Panel on Climate Change, Intergovernmental Panel on Climate Change, Geneva, Switzerland, https://doi.org/10.1017/9781009157896, 2021.

IPCC: in: Climate Change 2023: Synthesis Report. Contribution of Working Groups I, II and III to the Sixth Assessment Report of the Intergovernmental Panel on Climate Change, edited by: Core Writing Team, H. L. a. J. R. e., Switzerland, 35–115, https://doi.org/10.59327/IPCC/AR6-9789291691647, 2023.

Jacob, D. J., Turner, A. J., Maasakkers, J. D., Sheng, J., Sun, K., Liu, X., Chance, K., Aben, I., McKeever, J., and Frankenberg, C.: Satellite observations of atmospheric methane and their value for quantifying methane emissions, Atmos. Chem. Phys., 16, 14371–14396, https://doi.org/10.5194/acp-16-14371-2016, 2016.

Ji, D., Zhou, M., Wang, P., Yang, Y., Wang, T., Sun, X., Hermans, C., Yao, B., and Wang, G.: Deriving Temporal and Vertical Distributions of Methane in Xianghe Using Ground-based Fourier Transform Infrared and Gas-analyzer Measurements, Advances in Atmospheric Sciences, 37, 597–607, https://doi.org/10.1007/s00376-020-9233-4, 2020.

Kuze, A., Suto, H., Nakajima, M., and Hamazaki, T.: Thermal and near infrared sensor for carbon observation Fourier-transform spectrometer on the Greenhouse Gases Observing Satellite for greenhouse gases monitoring, Appl. Opt., 48, 6716–6733, https://doi.org/10.1364/AO.48.006716, 2009.

Kuze, A., Suto, H., Shiomi, K., Kawakami, S., Tanaka, M., Ueda, Y., Deguchi, A., Yoshida, J., Yamamoto, Y., Kataoka, F., Taylor, T. E., and Buijs, H. L.: Update on GOSAT TANSO-FTS performance, operations, and data products after more than 6 years in space, Atmos. Meas. Tech., 9, 2445–2461, https://doi.org/10.5194/amt-9-2445-2016, 2016.

Laughner, J. L., Toon, G. C., Mendonca, J., Petri, C., Roche, S., Wunch, D., Blavier, J. F., Griffith, D. W. T., Heikkinen, P., Keeling, R. F., Kiel, M., Kivi, R., Roehl, C. M., Stephens, B. B., Baier, B. C., Chen, H., Choi, Y., Deutscher, N. M., DiGangi, J. P., Gross, J., Herkommer, B., Jeseck, P., Laemmel, T., Lan, X., McGee, E., McKain, K., Miller, J., Morino, I., Notholt, J., Ohyama, H., Pollard, D. F., Rettinger, M., Riris, H., Rousogenous, C., Sha, M. K., Shiomi, K., Strong, K., Sussmann, R., Té, Y., Velazco, V. A., Wofsy, S. C., Zhou, M., and Wennberg, P. O.: The Total Carbon Column Observing Network's GGG2020 data version, Earth Syst. Sci. Data, 16, 2197–2260, https://doi.org/10.5194/essd-16-2197-2024, 2024.

Li, Z., Xia, X., Cribb, M., Mi, W., Holben, B., Wang, P., Chen, H., Tsay, S.-C., Eck, T. F., Zhao, F., Dutton, E. G., and Dickerson, R. E.: Aerosol optical properties and their radiative effects in northern China, Journal of Geophysical Research: Atmospheres, 112, https://doi.org/10.1029/2006JD007382, 2007.

Li, Z. Q., Xu, H., Li, K. T., Li, D. H., Xie, Y. S., Li, L., Zhang, Y., Gu, X. F., Zhao, W., Tian, Q. J., Deng, R. R., Su, X. L., Huang, B., Qiao, Y. L., Cui, W. Y., Hu, Y., Gong, C. L., Wang, Y. Q., Wang, X. F., Wang, J. P., Du, W. B., Pan, Z. Q., Li, Z. Z., and Bu, D.: Comprehensive Study of Optical, Physical, Chemical, and Radiative Properties of Total Columnar Atmospheric Aerosols over China: An Overview of Sun–Sky Radiometer Observation Network (SONET) Measurements, Bulletin of the American Meteorological Society, 99, 739–755, https://doi.org/10.1175/BAMS-D-17-0133.1, 2018.

Lloret, Z., Chevallier, F., and Cozic, A.: Refining the Global Picture: the Impact of Increased Resolution on CO_2 Atmospheric Inversions using OCO-2 XCO_2 retrievals, Authorea Preprints, https://doi.org/10.22541/au.171052488.85903583/v1, 2024.

Lorente, A., Borsdorff, T., Martinez-Velarte, M. C., Butz, A., Hasekamp, O. P., Wu, L., and Landgraf, J.: Evaluation of the methane full-physics retrieval applied to TROPOMI ocean sun glint measurements, Atmos. Meas. Tech., 15, 6585–6603, https://doi.org/10.5194/amt-15-6585-2022, 2022.

Noël, S., Reuter, M., Buchwitz, M., Borchardt, J., Hilker, M., Bovensmann, H., Burrows, J. P., Di Noia, A., Suto, H., Yoshida, Y., Buschmann, M., Deutscher, N. M., Feist, D. G., Griffith, D. W. T., Hase, F., Kivi, R., Morino, I., Notholt, J., Ohyama, H., Petri, C., Podolske, J. R., Pollard, D. F., Sha, M. K., Shiomi, K., Sussmann, R., Té, Y., Velazco, V. A., and Warneke, T.: XCO2 retrieval for GOSAT and GOSAT-2 based on the FOCAL algorithm, Atmos. Meas. Tech., 14, 3837–3869, https://doi.org/10.5194/amt-14-3837-2021, 2021.

Noël, S., Reuter, M., Buchwitz, M., Borchardt, J., Hilker, M., Schneising, O., Bovensmann, H., Burrows, J. P., Di Noia, A., Parker, R. J., Suto, H., Yoshida, Y., Buschmann, M., Deutscher, N. M., Feist, D. G., Griffith, D. W. T., Hase, F., Kivi, R., Liu, C., Morino, I., Notholt, J., Oh, Y.-S., Ohyama, H., Petri, C., Pollard, D. F., Rettinger, M., Roehl, C., Rousogenous, C., Sha, M. K., Shiomi, K., Strong, K., Sussmann, R., Té, Y., Velazco, V. A., Vrekoussis, M., and Warneke, T.: Retrieval of greenhouse gases from GOSAT and GOSAT-2 using the FOCAL algorithm, Atmospheric Measurement Techniques, 15, 3401–3437, https://doi.org/10.5194/amt-15-3401-2022 2022.

Oshchepkov, S., Bril, A., and Yokota, T.: PPDF-based method to account for atmospheric light scattering in observations of carbon dioxide from space, Journal of Geophysical Research: Atmospheres, 113, https://doi.org/10.1029/2008JD010061, 2008.

Parker, R. J., Boesch, H., Byckling, K., Webb, A. J., Palmer, P. I., Feng, L., Bergamaschi, P., Chevallier, F., Notholt, J., Deutscher, N., Warneke, T., Hase, F., Sussmann, R., Kawakami, S., Kivi, R., Griffith, D. W. T., and Velazco, V.: Assessing 5 years of GOSAT Proxy XCH₄ data and associated uncertainties, Atmos. Meas. Tech., 8, 4785–4801, https://doi.org/10.5194/amt-8-4785-2015, 2015.

Parker, R. J., Webb, A., Boesch, H., Somkuti, P., Barrio Guillo, R., Di Noia, A., Kalaitzi, N., Anand, J. S., Bergamaschi, P., Chevallier, F., Palmer, P. I., Feng, L., Deutscher, N. M., Feist, D. G., Griffith, D. W. T., Hase, F., Kivi, R., Morino, I., Notholt, J., Oh, Y. S., Ohyama, H., Petri, C., Pollard, D. F., Roehl, C., Sha, M. K., Shiomi, K., Strong, K., Sussmann, R., Té, Y., Velazco, V. A., Warneke, T., Wennberg, P. O., and Wunch, D.: A decade of GOSAT Proxy satellite CH4 observations, Earth Syst. Sci. Data, 12, 3383–3412, https://doi.org/10.5194/essd-12-3383-2020, 2020.

Peters, W., Jacobson, A. R., Sweeney, C., Andrews, A. E., Conway, T. J., Masarie, K., Miller, J. B., Bruhwiler, L. M. P., Pétron, G., Hirsch, A. I., Worthy, D. E. J., van der Werf, G. R., Randerson, J. T., Wennberg, P. O., Krol, M. C., and Tans, P. P.: An atmospheric perspective on North American carbon dioxide exchange: CarbonTracker, Proceedings of the National Academy of Sciences, 104, 18925–18930, https://doi.org/10.1073/pnas.0708986104, 2007.

Predybaylo, E., Lelieveld, J., Pozzer, A., Gromov, S., Zimmermann, P., Osipov, S., Klingmüller, K., Steil, B., Stenchikov, G., and McCabe, M.: Surface temperature and ozone responses to the 2030 Global Methane Pledge, Climatic Change, 178, 78, https://doi.org/10.1007/s10584-025-03908-5, 2025.

Ran, L., Deng, Z. Z., Wang, P. C., and Xia, X. A.: Black carbon and wavelength-dependent aerosol absorption in the North China Plain based on two-year aethalometer measurements, Atmospheric Environment, 142, 132–144, https://doi.org/10.1016/j.atmosenv.2016.07.014, 2016.

Reuter, M., Buchwitz, M., Schneising, O., Noël, S., Bovensmann, H., Burrows, J. P., Boesch, H., Di Noia, A., Anand, J., Parker, R. J., Somkuti, P., Wu, L., Hasekamp, O. P., Aben, I., Kuze, A., Suto, H., Shiomi, K., Yoshida, Y., Morino, I., Crisp, D., O'Dell, C. W., Notholt, J., Petri, C., Warneke, T., Velazco, V. A., Deutscher, N. M., Griffith, D. W. T., Kivi, R., Pollard, D. F., Hase, F., Sussmann, R., Té, Y. V., Strong, K., Roche, S., Sha, M. K., De Mazière, M., Feist, D. G., Iraci, L. T., Roehl, C. M., Retscher, C., and Schepers, D.: Ensemble-based satellite-derived carbon dioxide and methane column-averaged dry-air mole fraction data sets (2003–2018) for carbon and climate applications, Atmos. Meas. Tech., 13, 789–819, https://doi.org/10.5194/amt-13-789-2020, 2020.

Schepers, D., Guerlet, S., Butz, A., Landgraf, J., Frankenberg, C., Hasekamp, O., Blavier, J. F., Deutscher, N. M., Griffith, D. W. T., Hase, F., Kyro, E., Morino, I., Sherlock, V., Sussmann, R., and Aben, I.: Methane retrievals from Greenhouse Gases Observing Satellite (GOSAT) shortwave infrared measurements: Performance comparison of proxy and physics retrieval algorithms, Journal of Geophysical Research: Atmospheres, 117, https://doi.org/10.1029/2012JD017549, 2012.

Schneising, O., Buchwitz, M., Burrows, J. P., Bovensmann, H., Reuter, M., Notholt, J., Macatangay, R., and Warneke, T.: Three years of greenhouse gas column-averaged dry air mole fractions retrieved from satellite – Part 1: Carbon dioxide, Atmos. Chem. Phys., 8, 3827–3853, https://doi.org/10.5194/acp-8-3827-2008, 2008.

Schneising, O., Buchwitz, M., Reuter, M., Bovensmann, H., Burrows, J. P., Borsdorff, T., Deutscher, N. M., Feist, D. G., Griffith, D. W., and Hase, F.: A scientific algorithm to simultaneously retrieve carbon monoxide and methane from TROPOMI onboard Sentinel-5 Precursor, Atmospheric Measurement Techniques, 12, 6771–6802, https://doi.org/10.5194/amt-12-6771-2019, 2019.

Shen, N., Tan, J., Wang, W., Xue, W., Wang, Y., Huang, L., Yan, G., Song, Y., and Li, L.: Long-term changes of methane emissions from rice cultivation during 2000 – 2060 in China: Trends, driving factors, predictions and policy implications, Environment International, 191, 108958, https://doi.org/10.1016/j.envint.2024.108958, 2024.

Tian, Y., Hong, X., Shan, C., Sun, Y., Wang, W., Zhou, M., Wang, P., Lin, P., and Liu, C.: Investigating the Performance of Carbon Monoxide and Methane Observations from Sentinel-5 Precursor in China, https://doi.org/10.3390/rs14236045,   2022.

Toon, G., Blavier, J.-F., Washenfelder, R., Wunch, D., Keppel-Aleks, G., Wennberg, P., Connor, B., Sherlock, V., Griffith, D., Deutscher, N., and Notholt, J.: Total Column Carbon Observing Network (TCCON), in: Advances in Imaging, Vancouver, 26 April 2009, JMA3,

UNEP: Global Methane Assessment: Benefits and Costs of Mitigating Methane Emissions, United Nations Environment Programme, Nairobi, Kenya, 2021.

van Soest, H. L., den Elzen, M. G. J., and van Vuuren, D. P.: Net-zero emission targets for major emitting countries consistent with the Paris Agreement, Nature Communications, 12, https://doi.org/10.1038/s41467-021-22294-x, 2021.

Wang, W., Tian, Y., Liu, C., Sun, Y., Liu, W., Xie, P., Liu, J., Xu, J., Morino, I., Velazco, V. A., Griffith, D. W. T., Notholt, J., and Warneke, T.: Investigating the performance of a greenhouse gas observatory in Hefei, China, Atmos. Meas. Tech., 10, 2627–2643, https://doi.org/10.5194/amt-10-2627-2017, 2017.

WMO: State of the Global Climate 2024, World Meteorological Organization, Geneva, SwitzerlandWMO-No. 1368, 42, 2025.

WMO: State of the Global Climate 2025, World Meteorological Organization, Geneva, SwitzerlandWMO-No. 1391, 46, https://doi.org/10.59327/WMO/S/CRI/SOC/1, 2026.

Wu, L. H.: Product User Guide and Specification (PUGS) – ANNEX C for product CH4_GOS_SRPR (v2.3.9, 2009-mid2020), SRON Netherlands Institute for Space Research, Netherlands, 2021a.

Wu, L. H.: Algorithm Theoretical Basis Document (ATBD) – ANNEX C for product CH4_GOS_SRPR (v2.3.9, 2009-mid2020), SRON Netherlands Institute for Space Research, Groningen, 2021b.

Wunch, D., Toon, G. C., Sherlock, V., Deutscher, N. M., Liu, C., Feist, D. G., and Wennberg, P. O.: The Total Carbon Column Observing Network's GGG2014 Data Version, CaltechDATA, Pasadena, California, https://doi.org/10.14291/TCCON.GGG2014.DOCUMENTATION.R0/1221662, 2015.

Wunch, D., Toon, G. C., Wennberg, P. O., Wofsy, S. C., Stephens, B. B., Fischer, M. L., Uchino, O., Abshire, J. B., Bernath, P., Biraud, S. C., Blavier, J. F. L., Boone, C., Bowman, K. P., Browell, E. V., Campos, T., Connor, B. J., Daube, B. C., Deutscher, N. M., Diao, M., Elkins, J. W., Gerbig, C., Gottlieb, E., Griffith, D. W. T., Hurst, D. F., Jiménez, R., Keppel-Aleks, G., Kort, E. A., Macatangay, R., Machida, T., Matsueda, H., Moore, F., Morino, I., Park, S., Robinson, J., Roehl, C. M., Sawa, Y., Sherlock, V., Sweeney, C., Tanaka, T., and Zondlo, M. A.: Calibration of the Total Carbon Column Observing Network using aircraft profile data, Atmos. Meas. Tech., 3, 1351–1362, https://doi.org/10.5194/amt-3-1351-2010, 2010.

Yang, Y., Zhou, M., Langerock, B., Sha, M. K., Hermans, C., Wang, T., Ji, D., Vigouroux, C., Kumps, N., Wang, G., De Mazière, M., and Wang, P.: New ground-based Fourier-transform near-infrared solar absorption measurements of XCO2, XCH4 and XCO at Xianghe, China, Earth Syst. Sci. Data, 12, 1679–1696, 10.5194/essd-12-1679-2020, 2020.

Yokota, T., Yoshida, Y., Eguchi, N., Ota, Y., Tanaka, T., Watanabe, H., and Maksyutov, S.: Global Concentrations of CO2 and CH4 Retrieved from GOSAT: First Preliminary Results, SOLA - Scientific Online Letters on the Atmosphere, 5, 160–163, https://doi.org/10.2151/sola.2009-041, 2009.

Zhou, M., Wang, P., Kumps, N., Hermans, C., and Nan, W.: TCCON data from Xianghe, China, Release GGG2020.R0 (R0), CaltechDATA [dataset], https://doi.org/10.14291/tccon.ggg2020.xianghe01.R0, 2022.